Local structure and dynamics in methylammonium, formamidinium and cesium tin(II) mixed−halide perovskites from ^{119}Sn solid−state NMR

Dominik J. Kubicki,[a,b] Daniel Prochowicz,[d] Elodie Salager,[f,g] Aydar Rakhmatullin,[f] Clare P. Grey*[b], Lyndon Emsley*[c], Samuel D. Stranks*[a,h]

[a]Cavendish Laboratory, Department of Physics, University of Cambridge, JJ Thomson Avenue, Cambridge, CB3 0HE, UK
[b]Department of Chemistry, University of Cambridge, Lensfield Road, Cambridge, CB2 1EW, UK
[c]Laboratory of Magnetic Resonance, Institute of Chemical Sciences and Engineering, Ecole Polytechnique Fédérale de Lausanne (EPFL), CH−1015 Lausanne, Switzerland
[d]Institute of Physical Chemistry, Polish Academy of Sciences, Kasprzaka 44/52, 01−224 Warsaw, Poland
[f]Conditions Extrêmes et Matériaux: Haute Température et Irradiation (CEMHTI), UPR 3079 CNRS, Université d'Orléans, 1D Avenue de la Recherche Scientifique, Orléans 45071, France
[g]Réseau sur le Stockage Electrochimique de l'Energie (RS2E), FR 3459 CNRS, 33 Rue Saint Leu, Amiens 80039, France
[h]Department of Chemical Engineering and Biotechnology, University of Cambridge, Philippa Fawcett Drive, Cambridge, CB3 0AS, UK

Supporting Information Placeholder

ABSTRACT: Organic−inorganic tin(II) halide perovskites have emerged as promising alternatives to lead halide perovskites in optoelectronic applications. While they suffer from considerably poorer performance and stability as compared to their lead analogues, their performance improvements have so far largely been driven by trial and error efforts due to a critical lack of methods to probe their atomic-level microstructure. Here, we identify the challenges and devise a ^{119}Sn solid-state NMR protocol for the determination of the local structure of mixed-cation and mixed-halide tin(II) halide perovskites as well as their degradation products and related phases. We establish that the longitudinal relaxation of ^{119}Sn can span 6 orders of magnitude in this class of compounds which makes judicious choice of experimental NMR parameters essential for reliable detection of various phases. We show that Cl/Br and I/Br mixed-halide perovskites form solid alloys in any ratio, while only limited mixing is possible for I/Cl compositions. We elucidate the degradation pathways of Cs-, MA- and FA-based tin(II) halides and show that degradation leads to highly disordered, qualitatively similar products, regardless of the A-site cation and halide. We detect the presence of metallic tin amongst the degradation products, which we suggest could contribute to the previously reported high conductivities in tin(II) halide perovskites. ^{119}Sn NMR chemical shifts are a sensitive probe of the halide coordination environment as well as of the A-site cation composition. Finally, we use variable-temperature multi-field relaxation measurements to quantify ion dynamics in $MASnBr_3$, establish activation energies for motion and show that this motion leads to spontaneous halide homogenization at room temperature whenever two different pure-halide perovskites are put in physical contact.

Introduction

Organic−inorganic halide perovskites (OIHPs) have emerged as a new class of materials for solar cells and light emission applications owing to the ease of solution processing, immunity to most defects and long charge carrier lifetimes which can be tuned by compositional engineering.[1,2] Following the first report of perovskite−based solar cells (PSC) a decade ago,[3] the field of perovskite−based photovoltaics has been developing at a very fast pace, now reaching power conversion efficiencies of over 25%.[1,4,5]

OIHPs are represented by the generic ABX_3 formula, in which *A* is typically a small cation such as methylammonium, ($CH_3NH_3^+$, MA), formamidinium ($CH_3(NH_2)_2^+$, FA) and/or cesium ions. The inorganic sublattice is composed of $[BX_6]^{4-}$ octahedra, where *B* is a divalent metal such as Pb^{2+}, Sn^{2+}, Ge^{2+} or a mixture of monovalent and trivalent metals (e.g. Ag^+ and In^{3+}) and *X* is a halide: I^-, Br^- or Cl^-. Lead halide perovskites exhibit considerably higher ambient stability and optoelectronic performance[6,7] as compared to the tin− and germanium−based analogues,[8,9] hence many of the solar cells with record efficiency are based on Pb^{2+}.[4,10,11] Tin−based materials (fig. 1), while providing lower bandgaps than their lead analogues, essential for tandem solar cells, suffer from easy oxidation and disproportionation which lead to self−doping, very short charge carrier lifetimes and in turn to poor power conversion efficiencies. These undesirable processes have been mitigated by introducing antioxidant additives such as SnF_2,[12] hydrazine,[13] hydrazinium,[14,15] β−tin,[16] potassium salt of hydroquinonesulfonic acid (KHQSA)[17], ascorbic acid,[18] and by A−/X−site compositional engineering,[19−23] leading to efficiencies approaching 10%. Iodide−chloride mixing has been a widely investigated problem in the field of lead halide perovskite photovoltaics since chloride doping leads to significantly improved thin film crystallinity and carrier diffusion lengths, [24–27] and considerable improvements have also been reported for chloride doping in tin(II) halide perovskite based solar cells.[28,29] However, to the best of our knowledge, there is no direct evidence for I/Cl mixing in the case of tin(II) halide perovskites.

Another strategy to stabilize tin(II)–based materials is the use of mixed–metal tin(II)–lead(II) halide perovskites which combine the advantageous optoelectronic properties of lead–based materials while providing band gaps of 1.2–1.3 eV which are close to the optimum required for all–perovskite tandem solar cells.[30–34]

The resulting materials are typically probed using diffraction–based methods, which provide information about long–range order, and optical spectroscopies to characterize their electronic properties. However, the atomic-level effect of various additives cannot be evaluated since there are currently no robust protocols for probing the local structure of multi-component tin(II) halide perovskites. Rapid degradation of tin(II) halide perovskites has been consistently observed in device studies,[35–37] and degradation mechanisms have been investigated using XRD, TGA and UV–Vis spectroscopy. However, once again, the atomic–level mechanism of degradation and the exact identity of the resulting species remain elusive.

Solid–state NMR has recently been shown to be the method of choice to determine local structure and dynamics in lead halide perovskites, which are uniquely amenable owing to the atomic–level and element–specific resolution of NMR.[38] In particular, solid–state NMR can be used to evidence A/B–site cation incorporation,[39–45] halide mixing,[46–49] doping–induced phase segregation processes,[40,41,43,46] to study interfacial passivation mechanisms,[50–52] cation and anion dynamics[39,53–59] and degradation processes[60]. The local structure of tin halide perovskites has been previously investigated in $CsSnBr_3$,[61] $MASnI_3$[62] and $FASnI_3$[62] using pair distribution function (PDF) analysis. Given the prevalence of tin NMR studies of other groups of materials, it is surprising that it has not yet been applied to tin(II) halide perovskites. We show that this problem is not trivial. To the best of our knowledge, the only example of applying solid–state MAS NMR to tin halide perovskites to date is a ^{1}H MAS NMR study of cation mixing in $FA_{1-x}MA_xSnBr_3$.[63] Solid–state ^{207}Pb NMR has recently provided an abundance of atomic–level information on lead halide perovskites,[46–48,60] and hence it is expected that tin NMR should be well suited to study tin analogues as well as mixed tin–lead materials.

Tin has three NMR–active isotopes: ^{115}Sn, ^{117}Sn and ^{119}Sn with natural abundance of 0.3%, 7.7% and 8.6%, respectively. All three isotopes have spin I = ½ and similar gyromagnetic ratios which renders ^{119}Sn the most receptive of the three, with a receptivity ca. 27 times that of ^{13}C. Solid-state tin NMR has been widely employed to study organotin compounds,[64] crystalline oxides and stannates,[65,66] porous networks,[67–69] sulphides[70,71], nitrides,[72] and all–inorganic semiconductors[73–75] Tin NMR is particularly sensitive to the difference between the +2[76,77] and +4[78] oxidation state with the corresponding chemical shifts differences on the order of several hundreds of ppm, as well as to the type of atom covalently bound to the tin site. ^{119}Sn chemical shifts span the range between 1000 and −2000 ppm for diamagnetic compounds and 7000–8000 ppm for tin metal.[79] Much larger ranges of shifts are seen for paramagnetic compounds.[66]

Here, we probe the atomic–level microstructure of single– and mixed–halide (I, Br, Cl) tin(II) halide perovskites, single and mixed A–site cation (Cs, MA, FA) tin(II) halide perovskites and tin(IV) non–perovskites phases using ^{119}Sn MAS NMR spectroscopy. We show that iodide–bromide and bromide–chloride mixtures form solid solutions for any I/Br and Br/Cl ratio. On the other hand, iodide–chloride compositions, while partially miscible, yield phase segregated mixtures of phases. We show how ^{119}Sn MAS NMR can be applied to study degradation pathways of tin(II) halide perovskites and that degradation typically leads to highly disordered SnO_2 and halostannates(IV). We have also detected traces of metallic tin in the degraded material. Three of the degradation products, FA_2SnI_6, MA_2SnI_6 and Cs_2SnI_6 have a ^{119}Sn chemical shift of −4818 ppm, −4684 ppm and −4518 ppm, respectively, values unprecedented in their magnitude for diamagnetic tin compounds. Further, we show that ^{119}Sn longitudinal relaxation times (T_1) in this class of compounds can span 6 orders of magnitude which makes the use of optimized experimental parameters essential for reliable detection of various phases. Finally, we use variable–temperature multi–field ^{119}Sn MAS NMR to quantify halide dynamics in $MASnBr_3$ and show that it leads to spontaneous halide mixing at room temperature.

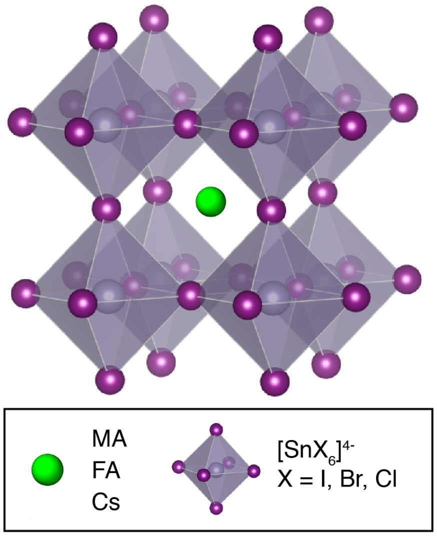

Figure 1. Schematic representation of the crystal structure of tin(II) halide perovskites formed by corner–sharing $[SnX_6]^{4-}$ octahedra.

Experimental

Materials. The following materials were used: methylammonium iodide (Sigma, 98%), formamidinium iodide (Sigma, 98%), formamidinium bromide (Sigma, 98%), formamidinium chloride (Sigma, 97%), CsI (Fischer, 99.9%), CsBr (Fischer, 99.9%), CsCl (Acros, 99.99%), SnI_2 (Sigma, 99.999%), $SnBr_2$ (Sigma), $SnCl_2$ (Sigma, 98%), SnI_4 (Sigma, 99.999%), $SnBr_4$ (Sigma, 99%).

Perovskite mechanosynthesis. The materials were prepared using mechanosynthesis[80,81] following recently published protocols.[82–84] The precursors were stored under argon. The halostannates were synthesized by grinding the reactants in an electric ball mill (Retsch MM–400) using an agate grinding jar (10 ml) and ball (⌀10 mm) for 30 minutes at 25 Hz. XRD patterns, SEM images and optical data of mechanochemical tin(II) halide perovskites have been previously reported[82,83] and agree with those recorded on materials prepared as single crystals and thin films. The quantities of reagents used in the synthesis are given in the SI.

NMR measurements. Solid–state MAS NMR spectra of ^{119}Sn (74.7 MHz) were recorded on a Bruker Avance III 4.7 T spectrometer equipped with a 4 mm MAS probe using 167 kHz RF strength. About 200-250 mg of sample was used for each measurement, corresponding to a full 4 mm rotor. The recycle delays were set based on the measured T_1 values, as described in the text. Low–temperature ^{1}H–^{13}C (125.8 MHz) CP MAS and room temperature ^{14}N (36.2 MHz) experiments were recorder on a Bruker Avance III 11.7 T spectrometer equipped with a 3.2 mm low–temperature CPMAS probe using previously optimized parameters.[39] High–temperature ^{119}Sn MAS NMR spectra were recorded on a Bruker Avance III 4.7 T spectrometer (74.7 MHz) using a 4 mm MAS Bruker probe (MgO stator) in the range between 308 K and 455 K using 4 mm zirconia rotors spinning at 5 kHz with heated nitrogen. High field data in the 308-474 K temperature range were obtained on a Bruker Avance III HD 17.6 T spectrometer (279.7 MHz) using a MAS LASER probe (Bruker) with airtight boron nitride crucibles contained in 7 mm zirconia rotors spinning at 6 kHz. Temperature was adjusted using diode laser heating.[85] The sample was sandwiched between two layers of ground KBr which allowed monitoring of the effective sample temperature through the ^{79}Br shift of KBr.[86,87] In order to prevent any interactions between KBr and the perovskite sample, a thin layer of PTFE tape was placed in between the two powders. Hahn-echoes of 40 μs total duration were used to mitigate ringing effects. CSA parameters were fitted using TopSpin 3.5. Further experimental details are given in the SI.

Results and discussion

Local structure of mixed–anion tin halostannates

Figure 2 shows ^{119}Sn solid–state MAS NMR spectra of methylammonium mixed–halide chloro– and bromostannates(II), bromostannate(IV) as well as their tin(II) and tin(IV) halide precursors recorded at room temperature. The ^{119}Sn chemical shift is highly sensitive to the local environment of the tin site and makes it possible to distinguish tin(II) precursors – $SnCl_2$ (−916 ppm, fig. 2a) and $SnBr_2$ (−640 ppm, fig. 2b) – from the corresponding perovskites – $MASnCl_3$ (−398 ppm, fig. 2c) and $MASnBr_3$ (−316 ppm (fig. 2g)). $MASnCl_3$ exhibits successive phase transitions at 283, 307, 331 and 463 K.[88] The structure adopted by $MASnCl_3$ under our experimental conditions (298 K) is monoclinic with slightly distorted $[SnCl_6]^{4-}$ octahedra which leads to the presence of chemical shift anisotropy (CSA) manifesting itself as a set of spinning sidebands (SSB) spaced by the MAS rotation frequency (fig. 2c). The fitted CSA parameters (δ_{CSA}=−435 ppm, η=0.26) are consistent with those previously reported.[88] Replacing Cl^- with Br^- in $MASnCl_3$ leads to solid solutions for the full range of Cl/Br ratios studied here. Low Br–concentrations, as in $MASnCl_{2.7}Br_{0.3}$, lead to a slight broadening and the appearance of two types of Sn(II) sites with similar CSA parameters (fig. 2d). The two sites correspond to different local $[SnBr_{6-x}Cl_x]^{4-}$ environments within the same phase, where the bromide content is higher for the environment at -351 ppm than it is for the environment at -393 ppm. As the concentration of Br^- in the lattice is increased, the resonance broadens further, takes on a chemical shift intermediate with respect to $MASnCl_3$ and $MASnBr_3$ and its apparent CSA becomes smaller (δ_{CSA}=−364 ppm, η=0.1 for $MASnCl_{2.1}Br_{0.9}$) (fig. 2e). $MASnBr_3$ is pseudocubic at room temperature so its δ_{CSA}≈0 ppm and there are no SSBs associated with the main peak (fig. 2g).[36] The peak is significantly broader than that of $MASnCl_3$ and $MASnCl_{1.5}Br_{1.5}$. We attribute these line width variations to the interference between CSA and fast halide hopping as discussed further in the text below (see also Supplementary Note 1). Note that this spectrum was acquired with no rotor synchronization in the quasi–static (ν_r = 600 Hz) regime (16.7 μs echo delay) due to very fast T_2 relaxation. Using a rotor–synchronized echo delay (83.3 μs) leads to lower SNR but does not lead to the appearance of SSBs (fig. S1). Further, ^{119}Sn NMR makes it possible to distinguish between bromostannates(II) and (IV). While $SnBr_4$ (−659 ppm) is shifted only slightly with respect to $SnBr_2$ (−640 ppm), the difference between $MASnBr_3$ (−316 ppm) and MA_2SnBr_6 (−1990 ppm) is much more pronounced.

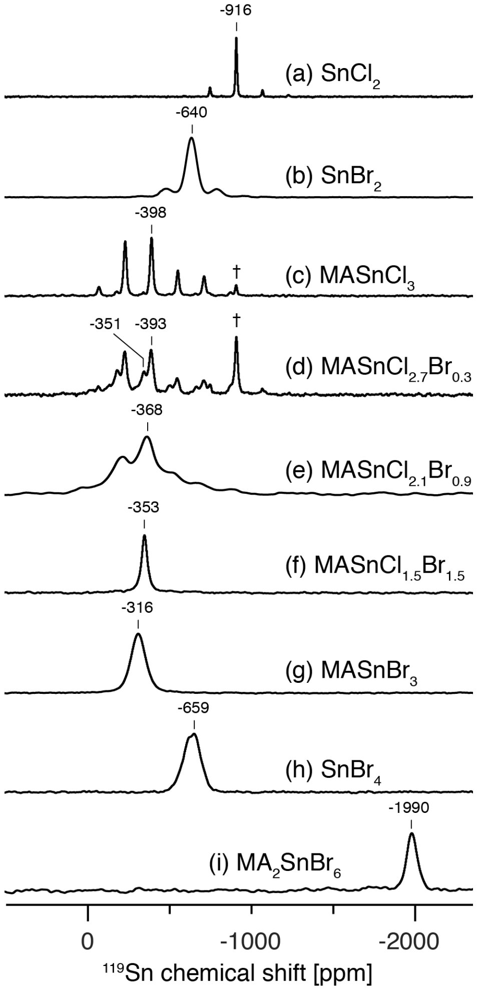

Figure 2. ^{119}Sn solid–state MAS NMR spectra of mixed–anion (chloride/bromide) halostannates and their precursors at 4.7 T, 12 kHz MAS (except for $SnBr_4$) and 298 K: (a) $SnCl_2$, (b) $SnBr_2$, (c) $MASnCl_3$, (d) $MASnCl_{2.7}Br_{0.3}$, (e) $MASnCl_{2.1}Br_{0.9}$, (f) $MASnCl_{1.5}Br_{1.5}$, (g) $MASnBr_3$, (h) $SnBr_4$ (at 0.6 kHz MAS to prevent melting), (i) MA_2SnBr_6. † indicates trace unreacted $SnCl_2$.

In turn, we investigate iodide–containing halostannate(II) and (IV) species. SnI_2 (−527 ppm fig. 3a) exhibits a partially resolved ^{119}Sn–^{127}I scalar coupling, $^1J_{Sn-I}$ = 6.2 kHz, similar in magnitude to the ^{207}Pb–^{127}I scalar coupling in PbI_2.[89] The crystal structure of $MASnI_3$ is pseudocubic at room temperature, hence a symmetric peak with δ_{CSA}≈0 ppm is expected. However, the material yields a very broad, slightly asymmetric resonance with a T_2^*≈10 μs (estimated from the line width) which we attribute to very efficient scalar relaxation. Similarly short T_2* has been previously observed in lead iodide perovskites.[46,49,90]

Figure 3c shows two ^{119}Sn spectra of $MASnCl_{2.7}I_{0.3}$: one obtained with a 50 ms recycle delay and the other with 50 s, to highlight the iodide– and chloride–rich environments, respectively. The signal corresponding to the iodide–rich phase is shifted to lower frequencies (to lower ppm values) with respect to pure $MASnI_3$ (fig. 3b), which supports the formation of $[SnI_{6-x}Cl_x]^{4-}$ coordination environments, thereby confirming that Cl^- can incorporate into the $MASnI_3$ perovskite lattice. On the other hand, the signal corresponding to the chloride–rich phase is identical, within experimental error, to that of pure $MASnCl_3$, (fig. 2c) which indicates that I^- has not been incorporated into the perovskite lattice of $MASnCl_3$. This result can be rationalized considering the difference in atomic radii of I^- (2.2 Å) and Cl^- (1.8 Å) which cause the $MASnCl_3$ structure to be more compact compared to that of $MASnI_3$.[36,88]

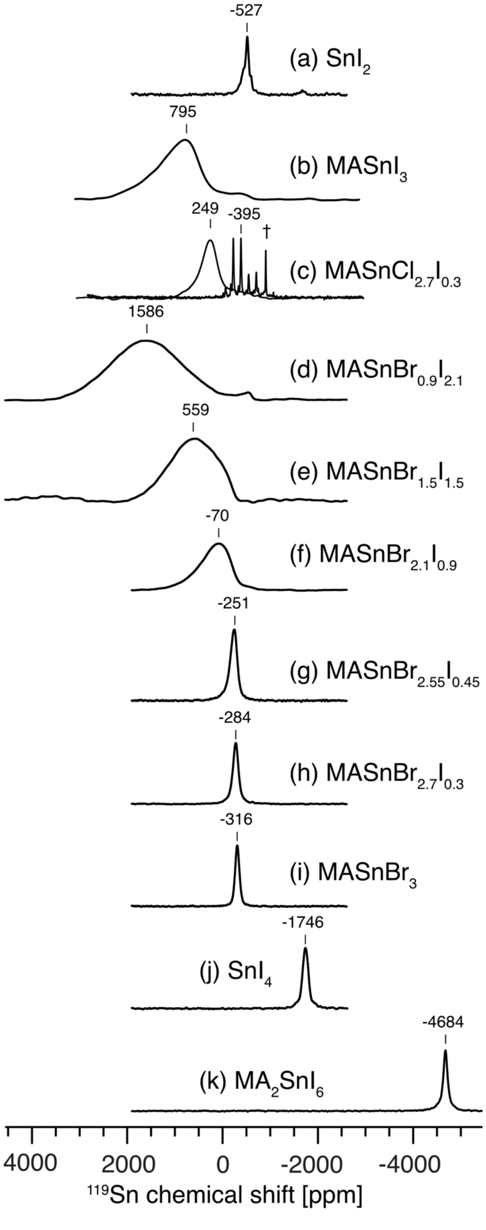

Figure 3. ^{119}Sn solid–state MAS NMR spectra of mixed–anion (iodide/chloride and iodide/bromide) halostannates and their precursors at 4.7 T, 12 kHz MAS and 298 K: (a) SnI_2, (b) $MASnI_3$, (c) $MASnCl_{2.7}I_{0.3}$, the signals at 249 and −395 ppm were detected with a recycle delay of 50 ms and 50 s, respectively (d) $MASnBr_{0.9}I_{2.1}$, (e) $MASnBr_{1.5}I_{1.5}$, (f) $MASnBr_{2.1}I_{0.9}$, (g) $MASnBr_{2.55}I_{0.45}$, (h) $MASnBr_{2.7}I_{0.3}$, (i) $MASnBr_3$, (j) SnI_4, (k) MA_2SnI_6. † indicates trace unreacted $SnCl_2$

On the other hand, iodide–bromide mixing has been previously studied in polycrystalline powders using X–ray diffraction and is expected due to the smaller difference in ionic radii of I^- (2.2 Å) and Br^- (2.0 Å).[36] As I^- is replaced by Br^- in the crystal structure of $MASnI_3$ (fig. 3b), the spectrum initially broadens and shifts to higher frequencies (to higher ppm values) ($MASnBr_{0.9}I_{2.1}$, fig. 3d), and then narrows and shifts to lower frequencies as the Br/I ratio increases further (above Br/I = 1.5:1.5, fig. 3e–f). Similar spectral trends have been previously reported in ^{119}Sn MAS NMR spectra of other disordered solids, such as stannate pyrochlores[91] and in ^{207}Pb MAS NMR spectra of mixed–cation lead halide perovskites[47,48]. Here, however, we ascribe the strong line width variation to the different magnitudes of ^{127}I and $^{79/81}$Br-induced relaxation, as described in the next section.

The difference in chemical shift between Sn(II) and Sn(IV) iodides and iodostannates in even more pronounced than for bromides and bromostannates. SnI_2 (−527 ppm, fig. 3a) can be easily distinguished from SnI_4 (−1746 ppm, fig. 3j) and the same is true for $MASnI_3$ (795 ppm, fig. 3b) and MA_2SnI_6 (−4684 ppm, fig. 3k). The latter ^{119}Sn chemical shift is, to the best of our knowledge, *the most shielded tin environment reported to date for a diamagnetic tin compound*. While based on the high electronegativity of iodine one might expect strong deshielding (shift at high positive ppm values), the exact opposite is observed experimentally. This is due to the effect of spin-orbit coupling which is important for heavy atoms, as has been previously shown by fully-relativistic DFT calculations.[92] The ^{119}Sn–^{127}I scalar coupling constant in molten SnI_4 has been previously found to be $^1J_{Sn-I}$ = 0.9 kHz and is not resolved in the solid state.[93]

Local structure of FA, Cs and mixed A–site cation tin halostannates

The A-site cation composition, mixing and segregation in solid lead halide perovskite has been previously explored directly using solid–state ^{1}H, ^{13}C and ^{133}Cs NMR as well as indirectly using ^{207}Pb NMR.[39–41,46,48,94] Here we show that the A-site composition in tin(II) halide perovskites can be probed indirectly using ^{119}Sn MAS NMR. Figure 4 shows ^{119}Sn MAS NMR spectra of single– and mixed–cation cesium, methylammonium and formamidinium tin(II) halides (I, Br, Cl). All iodides yield very broad (full width at half maximum (fwhm) of 70–170 kHz) and largely featureless spectra due to very efficient scalar T_2 relaxation (fig. 4a–c). At room temperature, $MASnI_3$ and $FASnI_3$ are pseudocubic[95] while $CsSnI_3$ is orthorhombic[96]. Whereas symmetric resonances are expected for highly symmetric structures, in this case the line shapes are asymmetric which suggests that they are not determined entirely by T_2 relaxation but rather that there is another contribution to the line shape. We believe that it is caused by the well-documented effect that a fast-relaxing quadrupolar nucleus has on the line shape of a spin-1/2 nucleus which is coupled to it.[97] We were able to numerically simulate the line shapes and obtained a good qualitative agreement with the experiment (fig. S7). Overall, high-sensitivity ^{119}Sn spectra can be recorded for 3D tin iodide perovskite within minutes under the experimental conditions used here and while they are sensitive to the halide coordination environment, their value for investigating A-site cation mixing is limited due to the lack of spectral resolution. Non-perovskite tin iodide phases (SnI_2, SnI_4 and MA_2SnI_6) do not suffer from this complication, likely owing to their different crystal structure in which the efficiency of this relaxation mechanism is reduced.

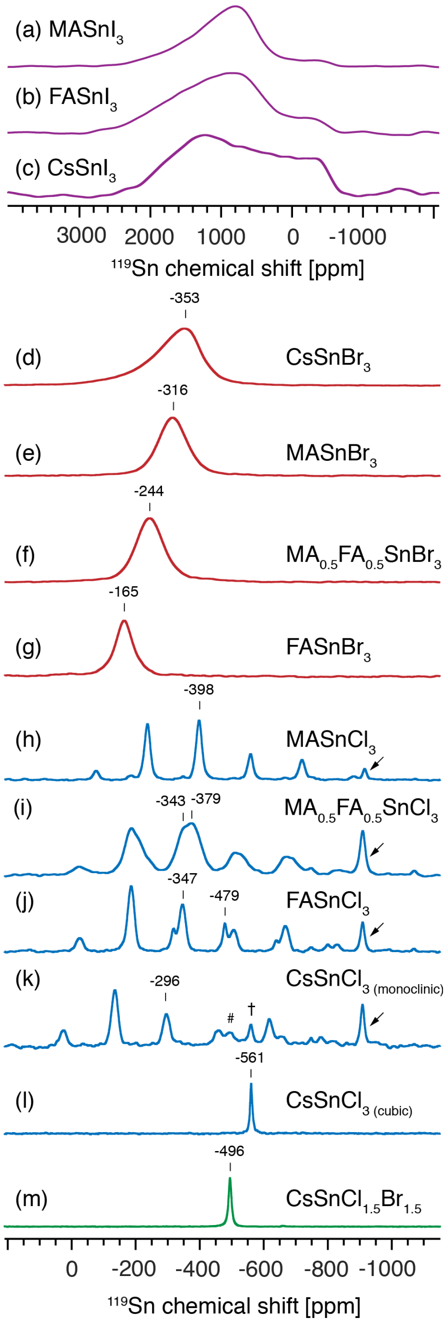

Figure 4. ^{119}Sn as a probe of the A−site cation (Cs, MA, FA) and A−site cation mixing in tin(II) halide perovskites. ^{119}Sn solid−state MAS NMR spectra at 4.7 T, 12 kHz MAS (unless stated otherwise) and 298 K of iodides: (a) $MASnI_3$, (b) $FASnI_3$ (static, see fig. S6 for 12 kHz MAS) (c) $CsSnI_3$; bromides: (d) $CsSnBr_3$, (e) $MASnBr_3$, (f) $MA_{0.5}FA_{0.5}SnBr_3$, (g) $FASnBr_3$; chlorides: (h) $MASnCl_3$, (i) $MA_{0.5}FA_{0.5}SnCl_3$, (j) $FASnCl_3$, (k) $CsSnCl_3$ (monoclinic), † indicates the metastable cubic phase of $CsPbI_3$, # is likely a second tin(II) site in the asymmetric unit cell of $CsPbCl_3$ (l) $CsSnCl_3$ (cubic); mixed−halides: (m) $CsSnCl_{1.5}Br_{1.5}$. The arrows indicate trace unreacted $SnCl_2$.

On the other hand, tin(II) bromide perovskites yield well-resolved spectra whereby the chemical shift is a sensitive fingerprint of the A-site cation (fig. 4d−g): $CsSnBr_3$ (−353 ppm), $MASnBr_3$ (−316 ppm), $FASnBr_3$ (−165 ppm). This makes it possible to probe A-site cation mixing using ^{119}Sn NMR in the bromide systems. For example, $MA_{0.5}FA_{0.5}SnBr_3$ (−244 ppm) yields a ^{119}Sn chemical shift which is intermediate with respect to the single A−site cation species. This leads to a linear correlation between the MA/FA ratio and the ^{119}Sn chemical shift in $MA_xFA_{1-x}SnBr_3$: $\delta_{Sn}(ppm)=-151\cdot x-166$. All four materials exist in the highest symmetry cubic α-phase at room temperature.[36,63,98] Also in this case, the line broadening was numerically simulated and is attributed to fast quadrupolar relaxation of $^{79/81}Br$ bound to ^{119}Sn (fig. S7).

Tin(II) chloride perovskites typically exist as low−symmetry phases at room temperature (monoclinic and triclinic for $CsSnCl_3$ and $MASnCl_3$, respectively[98,99]) hence they yield characteristic CSA patterns (fig. 4h−l). Also in this case the ^{119}Sn chemical shift is strongly dependent on the type of the A−site cation and an additional constraint is provided by the observed (298 K) CSA parameters: $MASnCl_3$ (δ_{iso}=−398 ppm, δ_{CSA}=−435 ppm, η=0.26), $FASnCl_3$ (δ_{iso}=−347 ppm, δ_{CSA}=−−508 ppm, η=0.06), $CsSnCl_3$ (δ_{iso}=−296 ppm, δ_{CSA}=−568 ppm, η=0.14). The spectrum of $FASnCl_3$ contains a second peak at $\delta_{iso=}$−479 ppm (δ_{CSA}=−401 ppm, η=0.08) which likely corresponds to a second tin(II) site inside the asymmetric unit cell, analogous to the situation observed in the low−symmetry phase of $MASnCl_3$.[88] A-site cation mixing leads to disorder which is exemplified by the spectrum of $MA_{0.5}FA_{0.5}SnCl_3$: the resonances broaden considerably and the two broad components (FA: δ_{iso}=−343, δ_{CSA}=−510 ppm, η=0.01 and MA: δ_{iso}=−379 ppm, δ_{CSA}=−353 ppm, η=0.12) take on values intermediate with respect to the single-cation phases. $CsSnCl_3$ can be trapped in its high−symmetry cubic phase (δ_{iso}=−561 ppm, δ_{CSA}≈0 ppm) at room temperature if the sample is briefly heated to 380 K (fig. 4l). This phase is metastable and can be transformed back to the low−symmetry phase in the presence of humidity.[98] Finally, we note that ^{119}Sn can be used to study the halide coordination environment in tin(II) halides perovskites not only when the A-site is an organic cation (fig. 2 and 3) but also when it is an inorganic cation such as cesium. Figure 4m shows that the ^{119}Sn chemical shift of $CsSnCl_{1.5}Br_{1.5}$ (−496 ppm) is intermediate with respect to the cubic phase of $CsSnCl_3$ (−561 ppm) and $CsSnBr_3$ (−353 ppm). Taken together, these findings demonstrate that ^{119}Sn MAS NMR is well-suited for probing the atomic-level microstructure of mixed-cation and mixed-anion tin(II) halide perovskites, as it is highly sensitive to both the A-site and X-site composition. The ^{119}Sn data can be complemented by ^{13}C, ^{14}N and ^{133}Cs NMR measurements to evaluate the local structure and dynamics of the A-site, as discussed further in the text.

Degradation pathways

Having established a comprehensive database of ^{119}Sn shifts for various relevant tin halide perovskite materials, we now explore degradation pathways in this class of compounds. Figure 5 shows a comparison between pristine and degraded $MASnBr_3$, $FASnBr_3$, $CsSnBr_3$, $MASnI_3$, $FASnI_3$ and $CsSnI_3$. The degradation was performed *ex situ* in air and the degradation conditions (temperature and duration) were chosen phenomenologically depending on the stability of different compounds, as monitored by the disappearance of the pristine perovskite ^{119}Sn signal.

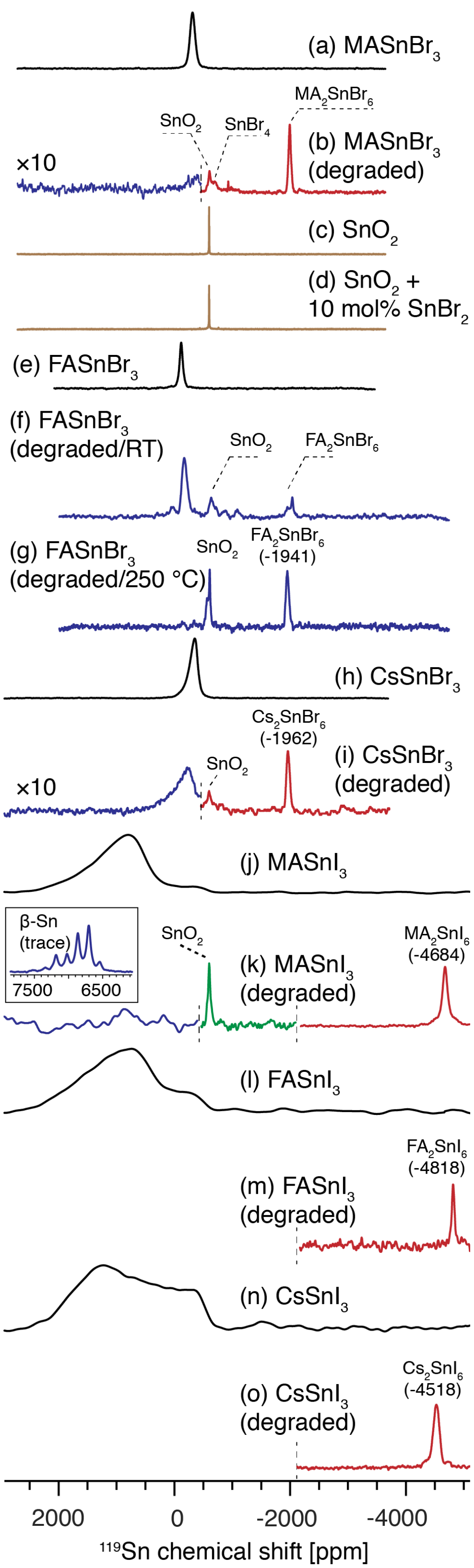

Figure 5. ^{119}Sn as a probe of tin(II) halide perovskite degradation. ^{119}Sn solid–state MAS NMR spectra at 4.7 T, 12 kHz MAS and 298 K of (a) $MASnBr_3$ (as prepared), (b) $MASnBr_3$ (degraded for 1 h at 250 °C in air), (c) SnO_2, (d) SnO_2 + 10 mol% $SnBr_2$ (ground and annealed at 250 °C in air), (e) $FASnBr_3$ (as prepared), (f) $FASnBr_3$ (degraded for 5 days at RT, in air), (g) $FASnBr_3$ (degraded for 0.5 h at 250 °C in air), (h) $CsSnBr_3$ (as prepared), (i) $CsSnBr_3$ (degraded for 0.5 h at 350 °C in air), (j) $MASnI_3$ (as prepared), (k) $MASnI_3$ (degraded for 1 h at 150 °C in air), (l) $FASnI_3$ (as prepared), (m) $FASnI_3$ (degraded for 1 h at RT in air), (n) $CsSnI_3$ (as prepared), (o) $CsSnI_3$ (degraded for 3 h at 100 °C in air). The dashed lines indicate points at which spectra acquired at different transmitter offsets were stitched together: b, i (two offsets), k (three offsets). For m and o only the high-field (low ppm) part was acquired.

Thermal degradation (1 h at 250 °C in air) of $MASnBr_3$ (fig. 5a) leads to a mixture of MA_2SnBr_6, SnO_2, $SnBr_4$ and trace amounts of species at −932 ppm, which we tentatively assign to an ionic product of the reaction between tin(II) and decomposition products of the organic cation. Interestingly, the SnO_2 signal in the degraded perovskite is significantly broader (fwhm: 3.5 kHz) compared to neat microcrystalline SnO_2 (fwhm: 0.2 kHz), which suggests that the SnO_2 formed during decomposition is locally highly disordered. This could be caused by bromide doping[100] or amorphization. We exclude bromide doping as the reason for the observed disorder, since a SnO_2 mechanochemically doped with $SnBr_2$ and annealed at the same temperature as the degradation process, did not lead to broadening of the SnO_2 resonance (fig. 5d). We therefore conclude that the SnO_2 formed during the degradation of tin(II) halides perovskites is poorly crystalline, or forms as nanodomains. We note that this would likely render its detection challenging by XRD.

We also observed that degradation under ambient conditions leads to qualitatively similar products as high-temperature degradation. However, the products formed at room temperature are considerably more locally disordered. Room-temperature degradation (5 days at RT, in air) of $FASnBr_3$ (fig. 5e) leads to very broad peaks of SnO_2 (fwhm: ~10 kHz) as well as FA_2SnBr_6 (two components, 3−6 kHz) (fig. 5f). After 5 days of exposure to ambient laboratory air, the sample of microcrystalline $FASnBr_3$ still contains a large amount of the non-degraded perovskite (~45% of the initial content). Degradation at 250 °C leads to complete disappearance of the perovskite phase and renders the peaks narrower (SnO_2: two components, fwhm 2−3 kHz, FA_2SnBr_6: fwhm 4 kHz), presumably as a result of thermal annealing (fig. 5g). Similarly, in the case of $CsSnBr_3$ degraded for 0.5 h at 350 °C in air we observe the formation of SnO_2 and Cs_2SnBr_6 (fig. 5h-i).

Analogous effects are observed during thermal degradation of $MASnI_3$ (fig. 5j−k) as well as $FASnI_3$ (fig. 5l−m) and $CsSnI_3$ (fig. 5n−o), which yield FA_2SnI_6 (−4818 ppm) and Cs_2SnI_6 (−4518 ppm), respectively. We have also acquired powder XRD diffraction on the degraded materials, which show the presence the oxidized A_2SnX_6 species (fig. S12). In addition, we note that we have detected metallic β-Sn in the sample of degraded $MASnI_3$ (fig. 5k, inset) which, however, is only present as a trace impurity (see table S4 for the necessary acquisition times). The anisotropic Knight shift of the β-Sn impurity is consistent with that of a reference β-Sn powder sample (δ_{iso}=6864 ppm or 0.68%, δ_{aniso}=486 ppm, η=0.1) and with the values previously reported for metallic tin powder[101,102] and thin films[79]. Interestingly, β-Sn has been recently used as an additive to increase the stability of $FASnI_3$.[16] We suggest that the presence of metallic tin in tin(II) halide perovskites among the degradation products may contribute to the high conductivity values previously reported in the literature for tin(II) halide perovskites, an effect to date attributed uniquely to self-doping. The formation of SnO_2 and SnX_4 has been shown in a recent TGA study,[103] which corresponds to the state in which the organic component has been fully volatilized. Solid-state ^{119}Sn NMR carried out on materials degraded under similar conditions refines this picture by showing that the degradation proceeds through an intermediate which is the corresponding tin(IV) halostannate, A_2SnX_6. The conclusions of our study are therefore fully consistent with those of Leijtens et al.[103] Based on these observations, we conclude that ^{119}Sn MAS is well-suited for studying degradation mechanisms in tin(II) halide perovskites.

Optimal experimental conditions for ^{119}Sn NMR detection

One of the most important considerations associated with the acquisition of ^{119}Sn MAS NMR data of tin(II) halides perovskites, their precursors and degradation products is that the ^{119}Sn longitudinal relaxation times (T_1) can span 6 orders of magnitude (fig. 6). This makes it essential to carefully adjust the experimental parameters so as to ensure optimal sensitivity and/or quantitativeness. The physical reason behind such a large spread of T_1 values is the difference in the dominating relaxation mechanism in different groups of tin compounds. T_1 relaxation in tin halides has been shown to be largely due to the ^{119}Sn−X scalar coupling whereby the relaxation rate depends on the coupling strength.[78,93] Since $^1J_{\text{Sn–I}} > {}^1J_{\text{Sn–Br}} > {}^1J_{\text{Sn–Cl}}$, it is expected that scalar relaxation is fastest in iodostannates, intermediate in bromostannates and slowest in chlorostannates.[78,93] This trend is clearly visible experimentally (fig. 6, blue). Beyond the coupling strength, the efficiency of scalar relaxation also depends on the rate at which the coupling is modulated (e.g. by fast relaxation of the halogen or chemical exchange). If these processes are not fast enough relative to the coupling strength, other mechanisms such as CSA or dipolar driven relaxation may prove more efficient. This is likely the case for $SnBr_2$, SnI_2, SnI_4 and MA_2SnBr_6 since these compounds have considerably longer T_1's as compared to the corresponding iodo- and bromostannates. Since $^1J_{\text{Sn–Cl}}$ are relatively small (<0.5 kHz),[93] it is possible that solid tin chlorides and chlorostannates are relaxed by these alternative processes.[78,93] Relaxation in tin metal (β−Sn) is driven by the conduction electrons, as shown by Korringa.[104] In the next section, we elucidate the relaxation mechanism for ^{119}Sn in $MASnBr_3$ and show that it is indeed determined by the scalar coupling to the halogen and driven by the motion of halides.

Complementarity with ^{13}C, ^{14}N and ^{133}Cs NMR

We note that the fast scalar relaxation does not affect the nuclei which are not directly bonded to the halogen. The scalar relaxation therefore has no effect on the A-site cation, which can be probed using high-resolution ^{1}H, ^{13}C, ^{133}Cs and ^{14}N MAS NMR, as we and others groups have previously shown for lead halide perovskites.[39–42,45,53,55,56] Figure S2 shows low-temperature ^{1}H−^{13}C CP spectra of methylammonium tin(II) single− and mixed−halide perovskites. The ^{13}C resonance of MA in the mixed−halide compositions is broader as compared to single halide compositions due to halide disorder. The ^{13}C resonances fall within a similar chemical shift range which makes the use of ^{119}Sn considerably more advantageous when elucidating the halide coordination environments. Figure S3 shows room-temperature ^{14}N MAS spectra of $MASnI_3$, $FASnI_3$ and $MA_{0.25}FA_{0.75}SnI_3$. We have previously shown that the width of the ^{14}N SSB manifold is related to the cubooctahedral symmetry in lead halide perovskites, with narrower manifolds corresponding to cubooctahedral symmetry closer to cubic; here we show that the same considerations hold for tin(II) halide perovskites. For example, the MA and FA SSB manifolds broaden in $MA_{0.25}FA_{0.75}SnI_3$ compared to the single-cation compositions indicating that the overall cubooctahedral symmetry has been reduced due to A-site cation mixing, similar to the effect previously observed in mixed-cation lead halide perovskites.[39] Finally, figure S4 shows room-temperature ^{133}Cs spectra of $CsSnX_3$ (X=I, Br, Cl). The signals are narrow (fwhm 90−110 Hz) and well-resolved which potentially makes ^{133}Cs MAS NMR well suited for studying component mixing and phase segregation processes in Cs-containing tin halide perovskites, similarly to how it has previously been shown in the context of lead halide perovskites.[40]

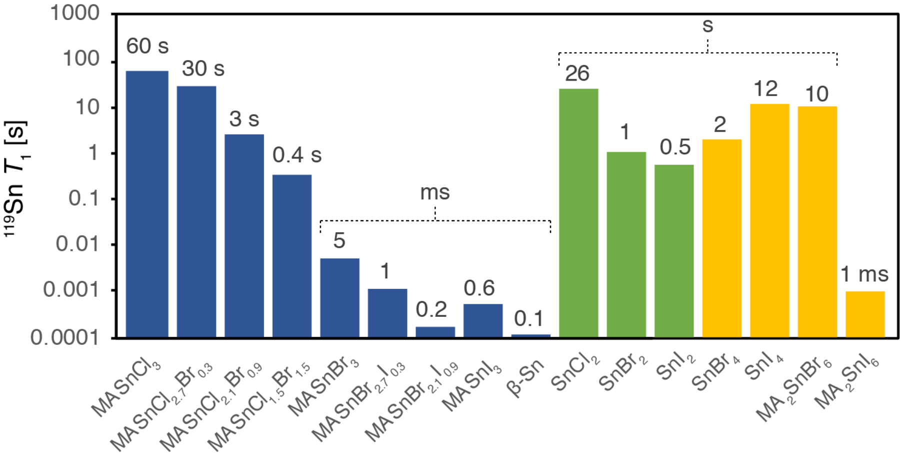

Figure 6. ^{119}Sn longitudinal relaxation times (T_1) at 4.7 T, 298 K, 12 kHz MAS (except for $SnBr_4$ which was measured at 0.6 kHz MAS to prevent melting) of the tin(II)− and tin(IV)−containing phases investigated in this work. Blue: tin(II) halide perovskites, green: tin(II) halides, yellow: tin(IV) halides and halostannates(IV). The numerical values are reported in table S3

Halide dynamics in $MASnBr_3$

NMR relaxation in solids is caused by fluctuating magnetic fields arising due to modulation of various interactions. It can therefore be used to study dynamic processes with timescales ranging from picoseconds to seconds.[105] We demonstrate this by using ^{119}Sn T_1 relaxation to probe the dynamic processes in $MASnBr_3$. The following mechanisms can in principle cause ^{119}Sn relaxation in solids: (a) dipole–dipole interaction,[106] (b) chemical shift anisotropy (CSA),[106] (c) Raman process,[107,108] (d) MAS–induced heteronuclear polarization exchange,[109] (d) scalar relaxation.[106]

In order to elucidate which mechanism is relevant in $MASnBr_3$, we acquired variable–temperature T_1 relaxation data at three magnetic field strengths: 4.7 T, 9.4 T, 17.6 T, and found that T_1 relaxation is essentially field independent (fig. 7b). The CSA mechanism has a strong field dependence hence can be excluded. Dipole-dipole relaxation leads to a T_1 minimum in the range of seconds (~5 s), hence this mechanism can also be excluded (see Supplementary Note 2 for the calculation). The Raman process leads to T_1 values which are independent of the magnetic field strength and inversely proportional to the square of the temperature, neither of which is the case here (fig. S5). MAS–induced heteronuclear polarization exchange arises due to crossing between energy levels of a spin−1/2 nucleus such as ^{119}Sn, ^{207}Pb or ^{199}Hg coupled to a quadrupolar spin with a very large quadrupolar coupling constant, which is the case for ^{127}I and $^{79/81}$Br. In this mechanism, the T_1 is significantly reduced when the sample is spun. We did not observe T_1 shortening between the static and spinning case (fig. S6). Finally, scalar relaxation is expected to be field independent and may be caused by modulation of the ^{119}Sn–$^{79/81}$Br scalar coupling either due to chemical exchange (scalar relaxation of the first kind) or fast quadrupolar relaxation of $^{79/81}$Br (scalar relaxation of the second kind).[106] The physical origin of the process can be determined from the temperature dependence of the T_2 relaxation times, which decrease with increasing temperature if they are caused by relaxation of the quadrupolar nucleus and increase with temperature if they are caused by chemical exchange, provided the system is in the extreme narrowing limit.[93] However, if the system is in the slow motion limit, both processes lead to longer ^{119}Sn T_2 as the temperature increases (see also Supplementary Note 3). We use fwhm of the ^{119}Sn signal as a measure of T_2 since we found it is field independent, hence it does not originate from a distribution of chemical environments (i.e. $T_2^* \approx T_2$) Experimentally, we observe that the ^{119}Sn resonances become narrower as the temperature increases (fig. 7a and table S1) which shows that T_2 increases with temperature. Since determining the relaxation regime for the quadrupolar partner is not straightforward in this case due to its very large quadrupole coupling constant,[110] we employ the determined activation energy as a constraint to identify the relevant relaxation mechanism. Plotting $\ln(^{119}\mathrm{Sn}\ T_1/\mathrm{s})$ as a function of the inverse temperature yields an Arrhenius plot (fig. 7b) from which we determine the activation energy of the process driving the relaxation (table 1 and S2). Averaging the results obtained at three magnetic fields and between 250–450 K, we obtain an average activation energy of (36 ± 6) kJ/mol or (0.37 ± 0.06) eV. This value is in fairly good agreement with those previously found for bromide diffusion in $MASnBr_3$ using ac and dc conductivity measurements (0.30 and 0.31 eV, respectively).[111,112] This value is also comparable to those previously reported for halide diffusion in α–SnI_2 (0.29 eV) and $MAPbI_3$ ((0.29 ± 0.06) eV). This result suggests that T_1 relaxation of ^{119}Sn in $MASnBr_3$ is primarily driven by scalar relaxation of the first kind, i.e. by movement of species inside the crystal lattice. Scalar relaxation of the second kind, on the other hand, would lead to activation energies corresponding to the process driving quadrupolar relaxation of $^{79/81}$Br, i.e. vibrational modes of the lattice, which are active in the far infrared to terahertz regime (<0.03 eV).[113,114] Since tin halides are ionic conductors,[115] we conclude that the chemical exchange process which drives ^{119}Sn relaxation in $MASnBr_3$ is the diffusion of Br^- ions in the crystal lattice. Ionic conductivity due to halides has been previously shown in lead halide perovskites[57,116] and tin halides.[115,117] These results confirm that $MASnBr_3$ is indeed an ionic conductor. DFT calculations predict a formation energy of 0.37 eV for iodide vacancies in $MASnI_3$ which is comparable to the experimentally measured ionic diffusion activation barrier. We note that although these two processes are not equivalent, halide migration relies on the presence of halide vacancies.[118]. Since $MASnBr_3$ starts decomposing above ~420 K and there is no T_1 minimum in the accessible temperature range, it was not possible to fit the full form of the relaxation process to access the halide diffusion rate. We note, however, that the previously calculated halide hopping rates are in the nanosecond range in lead halide perovskites.[119,120]

Finally, we show that the comparatively low activation energy for halide diffusion leads to spontaneous halide mixing at room temperature which can be conveniently probed using ^{119}Sn MAS NMR.

Table 1. Activation energies (E_a) for halide migration in tin(II) halide perovskites and related phases.

Material	E_a [kJ/mol]	E_a [eV]	Technique	Ref.
$MASnBr_3$ (4.7 T)	42.7 ± 0.5	0.44	solid–state NMR	this work
$MASnBr_3$ (9.4 T)	31.9 ± 0.1	0.33		
$MASnBr_3$ (17.6 T)	34.1 ± 0.1	0.35		
$MASnBr_3$ (average)[b]	36 ± 6	0.37 ± 0.06		
$MASnBr_3$	29.1	0.30	ac conductivity	111
$MASnBr_3$	30	0.31	dc conductivity	112
α–SnI_2	28	0.29	ac conductivity	115
$MASnI_3$	63	0.37 (V_I) 0.65 (I_i)[c]	DFT	118
$MAPbI_3$	28 ± 6	0.29 ± 0.06	transient ion–drift	116
$MAPbI_3$	16	0.17	^{127}I NQR	57

[a] The uncertainty is given as one standard deviation.

[c] Defect formation energy at the valence band maximum. V_I – iodide vacancy, I_i – iodide interstitial.

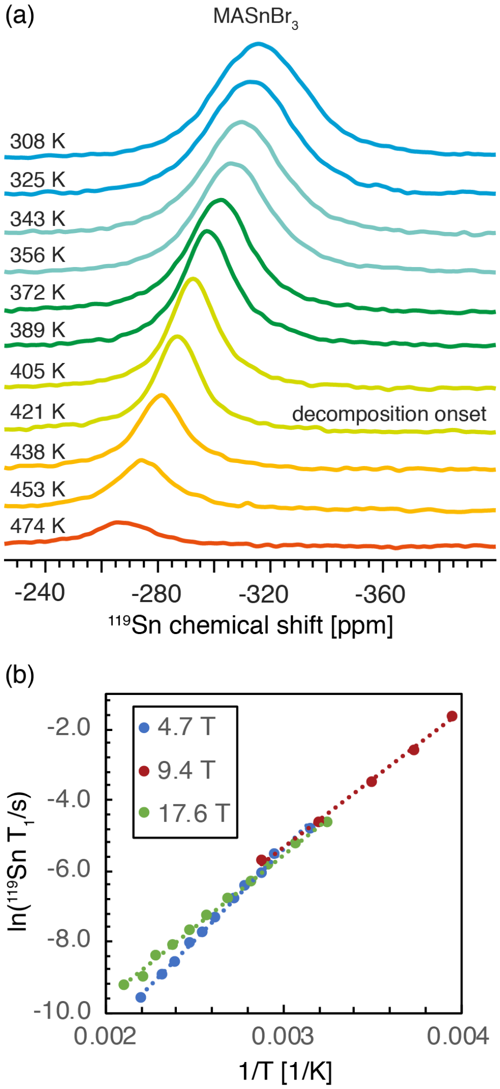

Figure 7. Halide dynamics in $MASnBr_3$ from multi–field variable–temperature ^{119}Sn solid–state MAS NMR. (a) variable–temperature (308–474 K) ^{119}Sn spectra at 17.6 T. All spectra were acquired using the same number of scans (4096) and are quantitative. The spectrum after thermal decomposition corresponds to MA_2SnBr_6 (fig. 4b) with traces of SnO_2 as discussed above. (b) An Arrhenius plot of the ^{119}Sn T_1 relaxation data at 4.7 T (blue), 9.4 T (red) and 17.6 T (green). The linear fits are indicated by dotted lines and the numerical values are given in table S2.

Spontaneous halide mixing

Thermally activated halide mixing has been previously demonstrated in microcrystalline[46] lead halide perovskites and in polycrystalline thin films[90,121]. In order to demonstrate this phenomenon in the context of tin(II) halide perovskites, we physically mixed equimolar amounts of microcrystalline $MASnBr_3$ (fig. 8a, –316 ppm) and $MASnCl_3$ (fig. 8b, –398 ppm) by weighing the materials into a vial and turning the vial upside down 5 times to provide light mixing. The spectrum recorded after 24 hours of storing the mixture under argon at room temperature shows that the single–halide perovskites have fully disappeared and a new chemical species has formed (fig. 8c,d). Recording a spectrum with a short recycle delay highlights the fast relaxing bromide–rich coordination environments (–325 ppm, fig. 8c) while using a long recycle delay accentuates the slowly relaxing chloride–rich environments (–340 ppm, fig. 8d). The resulting mixed–halide perovskite has a composition similar to that of $MASnCl_{1.5}Br_{1.5}$ (–353 ppm, fig. 8e) although the slight difference in chemical shifts demonstrates that the two materials are not identical. We expect these results to carry over to other tin(II) halide perovskite compositions and suggest that spontaneous halide mixing should occur whenever there is an intergranular halide concentration gradient.

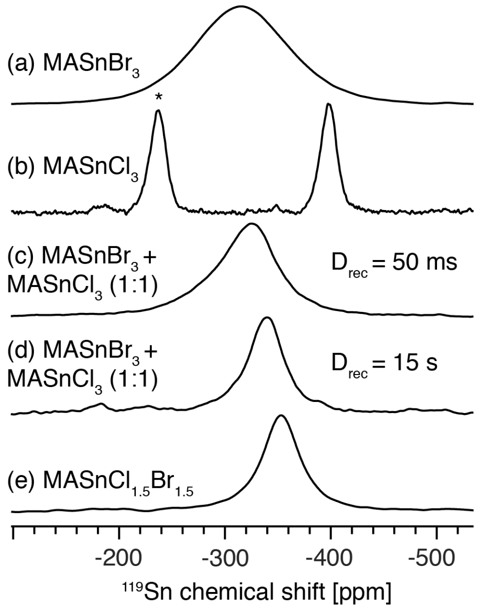

Figure 8. ^{119}Sn as a probe of spontaneous halide mixing. ^{119}Sn solid–state MAS NMR spectra at 4.7 T, 12 kHz MAS of (a) $MASnBr_3$, (b) $MASnCl_3$, the asterisk indicates a spinning sideband (c) 1:1 (mol/mol) mixture of $MASnBr_3$ and $MASnCl_3$, lightly mixed, recorded after 24 hours with a recycle delay of 50 ms, (d) same as (c) but using a recycle delay of 15 s to highlight the slowly relaxing chloride-rich environments, (e) $MASnCl_{1.5}Br_{1.5}$.

Conclusions

We have identified and overcome the challenges associated with the acquisition of solid–state ^{119}Sn MAS NMR data, namely that the longitudinal relaxation of ^{119}Sn in tin(II) halide perovskites and related materials spans 6 orders of magnitude, which makes it essential to judiciously choose the experimental parameters so as to obtain optimal results. We have shown that solid–state ^{119}Sn MAS NMR can be used to characterize the local structure of tin(II) mixed–halide and mixed A–site cation perovskite and related phases as well as to distinguish between tin(II) and tin(IV) halostannate phases. This property in particular can be employed to study degradation processes in tin(II) halide perovskites and we have exemplified it by identifying the degradation products of $MASnBr_3$, $FASnBr_3$, $CsSnBr_3$, $MASnI_3$, $FASnI_3$ and $CsSnI_3$. We have found that regardless of the composition, the decomposition products include amorphous SnO_2 and the corresponding tin(IV) halostannate, A_2SnX_6. Further, we have identified the dominant NMR relaxation mechanism of ^{119}Sn in solid $MASnBr_3$ as scalar relaxation of the first kind driven by bromide diffusion inside the perovskite lattice. We have quantified the activation energy of this process using variable–temperature multi–field relaxation measurements and found that the values are in excellent agreement with those extracted from previously reported electrical conductivity measurements. Finally, we have shown that spontaneous halide homogenization occurs at room temperature between microcrystalline single–halide tin(II) halide perovskites which leads to mixed–halide materials. We expect this property of tin(II) halide perovskite to carry over to other tin(II) halide perovskites systems featuring a halide concentration gradient. Taken together, we believe that ^{119}Sn MAS NMR is a general and versatile technique providing information on local structure and dynamics in tin(II) halide perovskites, complementary to the data obtained by diffraction techniques and optical spectroscopies.

Associated Content

Supporting Information

Supplementary information (additional ^{119}Sn, ^{13}C, ^{133}Cs and ^{14}N NMR spectra, numerical T_1 data, further experimental details), is available in the online version of the paper. Requests for additional data and correspondence should be addressed to C.P.G, L.E. or S.D.S.

Author Information

Corresponding Authors

*cpg27@cam.ac.uk
*lyndon.emsley@epfl.ch
*sds65@cam.ac.uk

Notes

SDS is a co-founder of Swift Solar, Inc.

Acknowledgement

This work has received funding from the European Union's Horizon 2020 research and innovation programme under the Marie Skłodowska-Curie grant agreement No. 841136. This work was supported by Swiss National Science Foundation Grant No. 200020_178860. D. P. acknowledges financial support from the HOMING programme of the Foundation for Polish Science co-financed by the European Union under the European Regional Development Fund (POIR.04.04.00-00-5EE7/18-00). Financial support from the IR-RMN-THC Fr3050 CNRS for conducting the research is gratefully acknowledged. S.D.S. acknowledges the Royal Society and Tata Group (UF150033).

References

(1) Li, W.; Wang, Z.; Deschler, F.; Gao, S.; Friend, R. H.; Cheetham, A. K. Chemically Diverse and Multifunctional Hybrid Organic–Inorganic Perovskites. *Nat. Rev. Mater.* **2017**, *2*, 16099.

(2) Jena, A. K.; Kulkarni, A.; Miyasaka, T. Halide Perovskite Photovoltaics: Background, Status, and Future Prospects. *Chem. Rev.* **2019**, *119* (5), 3036–3103. https://doi.org/10.1021/acs.chemrev.8b00539.

(3) Kojima, A.; Teshima, K.; Shirai, Y.; Miyasaka, Tsutomu. Organometal Halide Perovskites as Visible-Light Sensitizers for Photovoltaic Cells. *J. Am. Chem. Soc.* **2009**, *131*, 6050–6051.

(4) Yang, W. S.; Park, B.-W.; Jung, E. H.; Jeon, N. J.; Kim, Y. C.; Lee, D. U.; Shin, S. S.; Seo, J.; Kim, E. K.; Noh, J. H.; et al. Iodide Management in Formamidinium-Lead-Halide–Based Perovskite Layers for Efficient Solar Cells. *Science* **2017**, *356* (6345), 1376–1379. https://doi.org/10.1126/science.aan2301.

(5) Https://Www.Nrel.Gov/Pv/Cell-Efficiency.Html.

(6) Domanski, K.; Alharbi, E. A.; Hagfeldt, A.; Grätzel, M.; Tress, W. Systematic Investigation of the Impact of Operation Conditions on the Degradation Behaviour of Perovskite Solar Cells. *Nat. Energy* **2018**, *3* (1), 61–67. https://doi.org/10.1038/s41560-017-0060-5.

(7) Tress, W.; Domanski, K.; Carlsen, B.; Agarwalla, A.; Alharbi, E. A.; Graetzel, M.; Hagfeldt, A. Performance of Perovskite Solar Cells under Simulated Temperature-Illumination Real-World Operating Conditions. *Nat. Energy* **2019**, *4* (7), 568–574. https://doi.org/10.1038/s41560-019-0400-8.

(8) Shi, Z.; Guo, J.; Chen, Y.; Li, Q.; Pan, Y.; Zhang, H.; Xia, Y.; Huang, W. Lead-Free Organic–Inorganic Hybrid Perovskites for Photovoltaic Applications: Recent Advances and Perspectives. *Adv. Mater.* **2017**, *29* (16), 1605005. https://doi.org/10.1002/adma.201605005.

(9) Leijtens, T.; Eperon, G. E.; Noel, N. K.; Habisreutinger, S. N.; Petrozza, A.; Snaith, H. J. Stability of Metal Halide Perovskite Solar Cells. *Adv. Energy Mater.* **2015**, *5* (20), 1500963. https://doi.org/10.1002/aenm.201500963.

(10) Yang, W. S.; Noh, J. H.; Jeon, N. J.; Kim, Y. C.; Ryu, S.; Seo, J.; Seok, S. I. High-Performance Photovoltaic Perovskite Layers Fabricated through Intramolecular Exchange. *Science* **2015**, *348* (6240), 1234–1237. https://doi.org/10.1126/science.aaa9272.

(11) Abdi-Jalebi, M.; Andaji-Garmaroudi, Z.; Cacovich, S.; Stavrakas, C.; Philippe, B.; Richter, J. M.; Alsari, M.; Booker, E. P.; Hutter, E. M.; Pearson, A. J.; et al. Maximizing and Stabilizing Luminescence from Halide Perovskites with Potassium Passivation. *Nature* **2018**, *555*, 497.

(12) Lee, S. J.; Shin, S. S.; Kim, Y. C.; Kim, D.; Ahn, T. K.; Noh, J. H.; Seo, J.; Seok, S. I. Fabrication of Efficient Formamidinium Tin Iodide Perovskite Solar Cells through SnF2–Pyrazine Complex. *J. Am. Chem. Soc.* **2016**, *138* (12), 3974–3977. https://doi.org/10.1021/jacs.6b00142.

(13) Song, T.-B.; Yokoyama, T.; Stoumpos, C. C.; Logsdon, J.; Cao, D. H.; Wasielewski, M. R.; Aramaki, S.; Kanatzidis, M. G. Importance of Reducing Vapor Atmosphere in the Fabrication of Tin-Based Perovskite Solar Cells. *J. Am. Chem. Soc.* **2017**, *139* (2), 836–842. https://doi.org/10.1021/jacs.6b10734.

(14) Tsarev, S.; Boldyreva, A. G.; Luchkin, S. Y.; Elshobaki, M.; Afanasov, M. I.; Stevenson, K. J.; Troshin, P. A. Hydrazinium-Assisted Stabilisation of Methylammonium Tin Iodide for Lead-Free Perovskite Solar Cells. *J. Mater. Chem. A* **2018**, *6* (43), 21389–21395. https://doi.org/10.1039/C8TA07699E.

(15) Li, F.; Zhang, C.; Huang, J.-H.; Fan, H.; Wang, H.; Wang, P.; Zhan, C.; Liu, C.-M.; Li, X.; Yang, L.-M.; et al. A Cation-Exchange Approach for the Fabrication of Efficient Methylammonium Tin Iodide Perovskite Solar Cells. *Angew. Chem.* **2019**, *131* (20), 6760–6764. https://doi.org/10.1002/ange.201902418.

(16) Gu, F.; Ye, S.; Zhao, Z.; Rao, H.; Liu, Z.; Bian, Z.; Huang, C. Improving Performance of Lead-Free Formamidinium Tin Triiodide Perovskite Solar Cells by Tin Source Purification. *Sol. RRL* **2018**, *2* (10), 1800136. https://doi.org/10.1002/solr.201800136.

(17) Tai, Q.; Guo, X.; Tang, G.; You, P.; Ng, T.-W.; Shen, D.; Cao, J.; Liu, C.-K.; Wang, N.; Zhu, Y.; et al. Antioxidant Grain Passivation for Air-Stable Tin-Based Perovskite Solar Cells. *Angew. Chem.* **2019**, *131* (3), 816–820. https://doi.org/10.1002/ange.201811539.

(18) Xu, X.; Chueh, C.-C.; Yang, Z.; Rajagopal, A.; Xu, J.; Jo, S. B.; Jen, A. K.-Y. Ascorbic Acid as an Effective Antioxidant Additive to Enhance the Efficiency and Stability of Pb/Sn-Based Binary Perovskite Solar Cells. *Nano Energy* **2017**, *34*, 392–398. https://doi.org/10.1016/j.nanoen.2017.02.040.

(19) Zhao, Z.; Gu, F.; Li, Y.; Sun, W.; Ye, S.; Rao, H.; Liu, Z.; Bian, Z.; Huang, C.; Sun, W. Mixed-Organic-Cation Tin Iodide for Lead-Free Perovskite Solar Cells with an Efficiency of 8.12. *Adv. Sci. Weinh. Baden-Wurtt. Ger.* **2017**, *4* (Copyright (C) 2018 U.S. National Library of Medicine.), 1700204.

(20) Jokar, E.; Chien, C.-H.; Tsai, C.-M.; Fathi, A.; Diau, E. W.-G. Robust Tin-Based Perovskite Solar Cells with Hybrid Organic Cations to Attain Efficiency Approaching 10%. *Adv. Mater.* **2019**, *31* (2), 1804835. https://doi.org/10.1002/adma.201804835.

(21) Kopacic, I.; Friesenbichler, B.; Hoefler, S. F.; Kunert, B.; Plank, H.; Rath, T.; Trimmel, G. Enhanced Performance of Germanium Halide Perovskite Solar Cells through Compositional Engineering. *ACS Appl. Energy Mater.* **2018**, *1* (2), 343–347. https://doi.org/10.1021/acsaem.8b00007.

(22) Liu, J.; Ozaki, M.; Yakumaru, S.; Handa, T.; Nishikubo, R.; Kanemitsu, Y.; Saeki, A.; Murata, Y.; Murdey, R.; Wakamiya, A. Lead-Free Solar Cells Based on Tin Halide Perovskite Films with High Coverage and Improved Aggregation. *Angew. Chem.* **2018**, *130* (40), 13405–13409. https://doi.org/10.1002/ange.201808385.

(23) Shao, S.; Liu, J.; Portale, G.; Fang, H.-H.; Blake, G. R.; Brink, G. H. ten; Koster, L. J. A.; Loi, M. A. Highly Reproducible Sn-Based Hybrid Perovskite Solar Cells with 9% Efficiency. *Adv. Energy Mater.* **2018**, *8* (4), 1702019. https://doi.org/10.1002/aenm.201702019.

(24) Stranks, S. D.; Eperon, G. E.; Grancini, G.; Menelaou, C.; Alcocer, M. J. P.; Leijtens, T.; Herz, L. M.; Petrozza, A.; Snaith, H. J. Electron-Hole Diffusion Lengths Exceeding 1 Micrometer in an Organometal Trihalide Perovskite Absorber. *Science* **2013**, *342* (6156), 341–344. https://doi.org/10.1126/science.1243982.

(25) Dong, Q.; Yuan, Y.; Shao, Y.; Fang, Y.; Wang, Q.; Huang, J. Abnormal Crystal Growth in CH3NH3PbI3−xClx Using a Multi-Cycle Solution Coating Process. *Energy Environ. Sci.* **2015**, *8* (8), 2464–2470. https://doi.org/10.1039/C5EE01179E.

(26) Yang, B.; Keum, J.; Ovchinnikova, O. S.; Belianinov, A.; Chen, S.; Du, M.-H.; Ivanov, I. N.; Rouleau, C. M.; Geohegan, D. B.; Xiao, K. Deciphering Halogen Competition in Organometallic Halide Perovskite Growth. *J. Am. Chem. Soc.* **2016**, *138* (15), 5028–5035. https://doi.org/10.1021/jacs.5b13254.

(27) Yang, B.; Brown, C. C.; Huang, J.; Collins, L.; Sang, X.; Unocic, R. R.; Jesse, S.; Kalinin, S. V.; Belianinov, A.; Jakowski, J.; et al. Enhancing Ion Migration in Grain Boundaries of Hybrid Organic–Inorganic Perovskites by Chlorine. *Adv. Funct. Mater.* **2017**, *27* (26), 1700749. https://doi.org/10.1002/adfm.201700749.

(28) Marshall, K. P.; Walker, M.; Walton, R. I.; Hatton, R. A. Enhanced Stability and Efficiency in Hole-Transport-Layer-Free CsSnI3 Perovskite Photovoltaics. *Nat. Energy* **2016**, *1*, 16178. https://doi.org/10.1038/NENERGY.2016.178.

(29) Marshall, K. P.; Walton, R. I.; Hatton, R. A. Tin Perovskite/Fullerene Planar Layer Photovoltaics: Improving the Efficiency and Stability of Lead-Free Devices. *J. Mater. Chem. A* **2015**, *3* (21), 11631–11640. https://doi.org/10.1039/c5ta02950c.

(30) Eperon, G. E.; Leijtens, T.; Bush, K. A.; Prasanna, R.; Green, T.; Wang, J. T.-W.; McMeekin, D. P.; Volonakis, G.; Milot, R. L.; May, R.; et al. Perovskite-Perovskite Tandem Photovoltaics with Optimized Band Gaps. *Science* **2016**, *354* (6314), 861–865. https://doi.org/10.1126/science.aaf9717.

(31) Prasanna, R.; Gold-Parker, A.; Leijtens, T.; Conings, B.; Babayigit, A.; Boyen, H.-G.; Toney, M. F.; McGehee, M. D. Band Gap Tuning via Lattice Contraction and Octahedral Tilting in Perovskite Materials for Photovoltaics. *J. Am. Chem. Soc.* **2017**, *139* (32), 11117–11124. https://doi.org/10.1021/jacs.7b04981.

(32) Zhao, B.; Abdi-Jalebi, M.; Tabachnyk, M.; Glass, H.; Kamboj, V. S.; Nie, W.; Pearson, A. J.; Puttisong, Y.; Gödel, K. C.; Beere, H. E.; et al. High Open-Circuit Voltages in Tin-Rich Low-Bandgap Perovskite-Based Planar Heterojunction Photovoltaics. *Adv. Mater.* **2017**, *29* (2), 1604744. https://doi.org/10.1002/adma.201604744.

(33) Rajagopal, A.; Yang, Z.; Jo, S. B.; Braly, I. L.; Liang, P.-W.; Hillhouse, H. W.; Jen, A. K.-Y. Highly Efficient Perovskite–Perovskite Tandem Solar Cells Reaching 80% of the Theoretical Limit in Photovoltage. *Adv. Mater.* **2017**, *29* (34), 1702140. https://doi.org/10.1002/adma.201702140.

(34) Leijtens, T.; Prasanna, R.; Bush, K. A.; Eperon, G. E.; Raiford, J. A.; Gold-Parker, A.; Wolf, E. J.; Swifter, S. A.; Boyd, C. C.; Wang, H.-P.; et al. Tin–Lead Halide Perovskites with Improved Thermal and Air Stability for Efficient All-Perovskite Tandem Solar Cells. *Sustain. Energy Fuels* **2018**, *2* (11), 2450–2459. https://doi.org/10.1039/C8SE00314A.

(35) Noel, N. K.; Stranks, S. D.; Abate, A.; Wehrenfennig, C.; Guarnera, S.; Haghighirad, A.-A.; Sadhanala, A.; Eperon, G. E.; Pathak, S. K.; Johnston, M. B.; et al. Lead-Free Organic-Inorganic Tin Halide Perovskites for Photovoltaic Applications. *Energy Environ. Sci.* **2014**, *7* (9), 3061–3068. https://doi.org/10.1039/c4ee01076k.

(36) Hao, F.; Stoumpos, C. C.; Cao, D. H.; Chang, R. P. H.; Kanatzidis, M. G. Lead-Free Solid-State Organic-Inorganic Halide Perovskite Solar Cells. *Nat. Photonics* **2014**, *8* (6), 489–494. https://doi.org/10.1038/nphoton.2014.82.

(37) Boyd, C. C.; Cheacharoen, R.; Leijtens, T.; McGehee, M. D. Understanding Degradation Mechanisms and Improving Stability of Perovskite Photovoltaics. *Chem. Rev.* **2019**, *119* (5), 3418–3451. https://doi.org/10.1021/acs.chemrev.8b00336.

(38) Franssen, W. M. J.; Kentgens, A. P. M. Solid–State NMR of Hybrid Halide Perovskites. *Solid State Nucl. Magn. Reson.* **2019**, *100*, 36–44. https://doi.org/10.1016/j.ssnmr.2019.03.005.

(39) Kubicki, D. J.; Prochowicz, D.; Hofstetter, A.; Péchy, P.; Zakeeruddin, S. M.; Grätzel, M.; Emsley, L. Cation Dynamics in Mixed-Cation (MA)x(FA)1−XPbI3 Hybrid Perovskites from Solid-State NMR. *J. Am. Chem. Soc.* **2017**, *139* (29), 10055–10061. https://doi.org/10.1021/jacs.7b04930.

(40) Kubicki, D. J.; Prochowicz, D.; Hofstetter, A.; Zakeeruddin, S. M.; Grätzel, M.; Emsley, L. Phase Segregation in Cs-, Rb- and K-Doped Mixed-Cation (MA)x(FA)1−XPbI3 Hybrid Perovskites from Solid-State NMR. *J. Am. Chem. Soc.* **2017**, *139* (40), 14173–14180. https://doi.org/10.1021/jacs.7b07223.

(41) Kubicki, D. J.; Prochowicz, D.; Hofstetter, A.; Saski, M.; Yadav, P.; Bi, D.; Pellet, N.; Lewiński, J.; Zakeeruddin, S. M.; Grätzel, M.; et al. Formation of Stable Mixed Guanidinium–Methylammonium Phases with Exceptionally Long Carrier Lifetimes for High-Efficiency Lead Iodide-Based Perovskite Photovoltaics. *J. Am. Chem. Soc.* **2018**, *140* (9), 3345–3351. https://doi.org/10.1021/jacs.7b12860.

(42) Kubicki, D. J.; Prochowicz, D.; Hofstetter, A.; Zakeeruddin, S. M.; Grätzel, M.; Emsley, L. Phase Segregation in Potassium-Doped Lead Halide Perovskites from 39K Solid-State NMR at 21.1 T. *J. Am. Chem. Soc.* **2018**, *140* (23), 7232–7238. https://doi.org/10.1021/jacs.8b03191.

(43) Kubicki, D. J.; Prochowicz, D.; Pinon, A.; Stevanato, G.; Hofstetter, A.; Zakeeruddin, S. M.; Grätzel, M.; Emsley, L. Doping and Phase Segregation in Mn2+- and Co2+-Doped Lead Halide Perovskites from 133Cs and 1H NMR Relaxation Enhancement. *J. Mater. Chem. A* **2019**, *7*, 2326–2333. https://doi.org/10.1039/C8TA11457A.

(44) Xiang, W.; Wang, Z.; Kubicki, D. J.; Tress, W.; Luo, J.; Prochowicz, D.; Akin, S.; Emsley, L.; Zhou, J.; Dietler, G.; et al. Europium-Doped CsPbI2Br for Stable and Highly Efficient Inorganic Perovskite Solar Cells. *Joule* **2019**, *3* (1), 205–214. https://doi.org/10.1016/j.joule.2018.10.008.

(45) Franssen, W. M. J.; Bruijnaers, B. J.; Portengen, V. H. L.; Kentgens, A. P. M. Dimethylammonium Incorporation in Lead Acetate Based MAPbI3 Perovskite Solar Cells. *ChemPhysChem* **2018**, *19* (22), 3107–3115. https://doi.org/10.1002/cphc.201800732.

(46) Rosales, B. A.; Men, L.; Cady, S. D.; Hanrahan, M. P.; Rossini, A. J.; Vela, Javier. Persistent Dopants and Phase Segregation in Organolead Mixed-Halide Perovskites. *Chem. Mater.* **2016**, *28*, 6848–6859. https://doi.org/10.1021/acs.chemmater.6b01874.

(47) Karmakar, A.; Askar, A. M.; Bernard, G. M.; Terskikh, V. V.; Ha, M.; Patel, S.; Shankar, K.; Michaelis, V. K. Mechanochemical Synthesis of Methylammonium Lead Mixed–Halide Perovskites: Unraveling the Solid-Solution Behavior Using Solid-State NMR. *Chem. Mater.* **2018**, *30*, 2309–2321. https://doi.org/10.1021/acs.chemmater.7b05209.

(48) Askar, A. M.; Karmakar, A.; Bernard, G. M.; Ha, M.; Terskikh, V. V.; Wiltshire, B. D.; Patel, S.; Fleet, J.; Shankar, K.; Michaelis, V. K. Composition-Tunable Formamidinium Lead Mixed Halide Perovskites via Solvent-Free Mechanochemical Synthesis: Decoding the Pb Environments Using Solid-State NMR Spectroscopy. *J. Phys. Chem. Lett.* **2018**, *9*, 2671–2677. https://doi.org/10.1021/acs.jpclett.8b01084.

(49) Hanrahan, M. P.; Men, L.; Rosales, B. A.; Vela, J.; Rossini, A. J. Sensitivity-Enhanced 207Pb Solid-State NMR Spectroscopy for the Rapid, Non-Destructive Characterization of Organolead Halide Perovskites. *Chem. Mater.* **2018**, *30* (20), 7005–7015. https://doi.org/10.1021/acs.chemmater.8b01899.

(50) Bi, D.; Li, X.; Milić, J. V.; Kubicki, D. J.; Pellet, N.; Luo, J.; LaGrange, T.; Mettraux, P.; Emsley, L.; Zakeeruddin, S. M.; et al. Multifunctional Molecular Modulators for Perovskite Solar

Cells with over 20% Efficiency and High Operational Stability. *Nat. Commun.* **2018**, *9* (1), 4482. https://doi.org/10.1038/s41467-018-06709-w.

(51) Alharbi, E. A.; Alyamani, A. Y.; Kubicki, D. J.; Uhl, A. R.; Walder, B. J.; Alanazi, A. Q.; Luo, J.; Burgos-Caminal, A.; Albadri, A.; Albrithen, H.; et al. Atomic-Level Passivation Mechanism of Ammonium Salts Enabling Highly Efficient Perovskite Solar Cells. *Nat. Commun.* **2019**, *10* (1), 1–9. https://doi.org/10.1038/s41467-019-10985-5.

(52) Tavakoli, M. M.; Tress, W.; Milić, J. V.; Kubicki, D.; Emsley, L.; Grätzel, M. Addition of Adamantylammonium Iodide to Hole Transport Layers Enables Highly Efficient and Electroluminescent Perovskite Solar Cells. *Energy Environ. Sci.* **2018**, *11* (11), 3310–3320. https://doi.org/10.1039/C8EE02404A.

(53) Wasylishen, R. E.; Knop, O.; Macdonald, J. B. Cation Rotation in Methylammonium Lead Halides. *Solid State Commun.* **1985**, *56* (7), 581–582. https://doi.org/10.1016/0038-1098(85)90959-7.

(54) Knop, O.; Wasylishen, R. E.; White, M. A.; Cameron, T. S.; Van Oort, M. J. M. Alkylammonium Lead Halides. Part 2. CH3NH3PbX3 (X = Chlorine, Bromine, Iodine) Perovskites: Cuboctahedral Halide Cages with Isotropic Cation Reorientation. *Can. J. Chem.* **1990**, *68* (Copyright (C) 2018 American Chemical Society (ACS). All Rights Reserved.), 412–422. https://doi.org/10.1139/v90-063.

(55) Franssen, W. M. J.; van Es, S. G. D.; Dervisoglu, R.; de Wijs, G. A.; Kentgens, A. P. M. Symmetry, Dynamics, and Defects in Methylammonium Lead Halide Perovskites. *J. Phys. Chem. Lett.* **2017**, *8*, 61–66. https://doi.org/10.1021/acs.jpclett.6b02542.

(56) Bernard, G. M.; Wasylishen, R. E.; Ratcliffe, C. I.; Terskikh, V.; Wu, Q.; Buriak, J. M.; Hauger, T. Methylammonium Cation Dynamics in Methylammonium Lead Halide Perovskites: A Solid-State NMR Perspective. *J. Phys. Chem. A* **2018**, *122* (6), 1560–1573. https://doi.org/10.1021/acs.jpca.7b11558.

(57) Senocrate, A.; Moudrakovski, I.; Kim, G. Y.; Yang, T.-Y.; Gregori, G.; Grätzel, M.; Maier, Joachim. The Nature of Ion Conduction in Methylammonium Lead Iodide: A Multimethod Approach. *Angew. Chem. Int. Ed.* **2017**, *56*, 7755–7759. https://doi.org/10.1002/anie.201701724.

(58) Senocrate, A.; Moudrakovski, I.; Maier, J. Short-Range Ion Dynamics in Methylammonium Lead Iodide by Multinuclear Solid State NMR and 127I NQR. *Phys. Chem. Chem. Phys.* **2018**, *20* (30), 20043–20055. https://doi.org/10.1039/C8CP01535J.

(59) Senocrate, A.; Moudrakovski, I.; Acartürk, T.; Merkle, R.; Kim, G. Y.; Starke, U.; Grätzel, M.; Maier, J. Slow CH3NH3+ Diffusion in CH3NH3PbI3 under Light Measured by Solid-State NMR and Tracer Diffusion. *J. Phys. Chem. C* **2018**, *122* (38), 21803–21806. https://doi.org/10.1021/acs.jpcc.8b06814.

(60) Askar, A. M.; Bernard, G. M.; Wiltshire, B.; Shankar, K.; Michaelis, V. K. Multinuclear Magnetic Resonance Tracking of Hydro, Thermal, and Hydrothermal Decomposition of CH3NH3PbI3. *J. Phys. Chem. C* **2017**, *121* (2), 1013–1024. https://doi.org/10.1021/acs.jpcc.6b10865.

(61) Fabini, D. H.; Laurita, G.; Bechtel, J. S.; Stoumpos, C. C.; Evans, H. A.; Kontos, A. G.; Raptis, Y. S.; Falaras, P.; Van der Ven, A.; Kanatzidis, M. G.; et al. Dynamic Stereochemical Activity of the Sn2+ Lone Pair in Perovskite CsSnBr3. *J. Am. Chem. Soc.* **2016**, *138* (36), 11820–11832. https://doi.org/10.1021/jacs.6b06287.

(62) Laurita, G.; H. Fabini, D.; C. Stoumpos, C.; G. Kanatzidis, M.; Seshadri, R. Chemical Tuning of Dynamic Cation Off-Centering in the Cubic Phases of Hybrid Tin and Lead Halide Perovskites. *Chem. Sci.* **2017**, *8* (8), 5628–5635. https://doi.org/10.1039/C7SC01429E.

(63) Ferrara, C.; Patrini, M.; Pisanu, A.; Quadrelli, P.; Milanese, C.; Tealdi, C.; Malavasi, L. Wide Band-Gap Tuning in Sn-Based Hybrid Perovskites through Cation Replacement: The FA(1-x)MA(x)SnBr(3) Mixed System. *J. Mater. Chem. A* **2017**, *5* (19), 9391–9395. https://doi.org/10.1039/c7ta01668a.

(64) Wrackmeyer, B. Application of 119Sn NMR Parameters. In *Annual Reports on NMR Spectroscopy*; Webb, G. A., Ed.; Academic Press, 1999; Vol. 38, pp 203–264. https://doi.org/10.1016/S0066-4103(08)60038-1.

(65) Clayden, N. J.; Dobson, C. M.; Fern, A. High-Resolution Solid-State Tin-119 Nuclear Magnetic Resonance Spectroscopy of Ternary Tin Oxides. *J. Chem. Soc. Dalton Trans.* **1989**, No. 5, 843–847. https://doi.org/10.1039/DT9890000843.

(66) Grey, C. P.; Dobson, C. M.; Cheetham, A. K.; Jakeman, R. J. B. Studies of Rare-Earth Stannates by Tin-119 MAS NMR. The Use of Paramagnetic Shift Probes in the Solid State. *J. Am. Chem. Soc.* **1989**, *111* (2), 505–511. https://doi.org/10.1021/ja00184a017.

(67) Lin, Z.; Rocha, J.; Jesus, J. D. P. de; Ferreira, A. Synthesis and Structure of a Novel Microporous Framework Stannosilicate. *J. Mater. Chem.* **2000**, *10* (6), 1353–1356. https://doi.org/10.1039/B000102N.

(68) Ferreira, A.; Lin, Z.; Rocha, J.; Morais, C. M.; Lopes, M.; Fernandez, C. Ab Initio Structure Determination of a Small-Pore Framework Sodium Stannosilicate. *Inorg. Chem.* **2001**, *40* (14), 3330–3335. https://doi.org/10.1021/ic0012571.

(69) Wolf, P.; Valla, M.; Rossini, A. J., Dr.; Comas-Vives, A., Dr.; Núñez-Zarur, F., Dr.; Malaman, B., Prof.; Lesage, A., Dr.; Emsley, L., Prof. Dr.; Copéret, C.; Hermans, I. NMR Signatures of the Active Sites in Sn-β Zeolite. *Angew. Chem. - Int. Ed.* **2014**, *53* (38), 10179–10183. https://doi.org/10.1002/anie.201403905.

(70) Mundus, C.; Taillades, G.; Pradel, A.; Ribes, M. A 119Sn Solid-State Nuclear Magnetic Resonance Study of Crystalline Tin Sulphides. *Solid State Nucl. Magn. Reson.* **1996**, *7* (2), 141–146. https://doi.org/10.1016/S0926-2040(96)01243-X.

(71) Pietrass, T.; Taulelle, F. 119Sn Solid-State NMR of Tin Sulfides. Evidence of Polytypism in SnS2. *Magn. Reson. Chem.* **1997**, *35* (6), 363–366. https://doi.org/10.1002/(SICI)1097-458X(199706)35:6<363::AID-OMR79>3.0.CO;2-P.

(72) Scotti, N.; Kockelmann, W.; Senker, J.; Traßel, S.; Jacobs, H. Sn3N4, ein Zinn(IV)-nitrid – Synthese und erste Strukturbestimmung einer binären Zinn–Stickstoff-Verbindung. *Z. Für Anorg. Allg. Chem.* **1999**, *625* (9), 1435–1439. https://doi.org/10.1002/(SICI)1521-3749(199909)625:9<1435::AID-ZAAC1435>3.0.CO;2-#.

(73) Grykałowska, A.; Nowak, B. High-Resolution Solid-State 119Sn and 195Pt NMR Studies of MPtSn Semiconductors (M=Ti, Zr, Hf, Th). *Solid State Nucl. Magn. Reson.* **2005**, *27* (4), 223–227. https://doi.org/10.1016/j.ssnmr.2004.11.006.

(74) Lock, H.; Xiong, J.; Wen, Y.-C.; Parkinson, B. A.; Maciel, G. E. Solid-State 29Si, 113Cd, 119Sn, and 31P NMR Studies of II-IV-P2 Semiconductors. *Solid State Nucl. Magn. Reson.* **2001**, *20* (3), 118–129. https://doi.org/10.1006/snmr.2001.0036.

(75) Protesescu, L.; Rossini, A. J.; Kriegner, D.; Valla, M.; De Kergommeaux, A.; Walter, M.; Kravchyk, K. V.; Nachtegaal, M.; Stangl, J.; Malaman, B.; et al. Unraveling the Core-Shell Structure of Ligand-Capped Sn/SnOx Nanoparticles by Surface-Enhanced Nuclear Magnetic Resonance, Mössbauer, and X-Ray Absorption Spectroscopies. *ACS Nano* **2014**, *8* (3), 2639–2648. https://doi.org/10.1021/nn406344n.

(76) Amornsakchai, P.; Apperley, D. C.; Harris, R. K.; Hodgkinson, P.; Waterfield, P. C. Solid-State NMR Studies of Some Tin(II) Compounds. *Recent Adv. Appl. Solid-State NMR Supercond. Phys. Mol. Biol.* **2004**, *26* (3), 160–171. https://doi.org/10.1016/j.ssnmr.2004.03.010.

(77) Yeh, H.-M. M.; Geanangel, R. A. 119Sn NMR Spectra of Tin(II) Halides. *Inorganica Chim. Acta* **1981**, *52*, 113–118. https://doi.org/10.1016/S0020-1693(00)88583-7.

(78) Sharp, R. R. Field Dependence of Nuclear Magnetic Relaxation of 119Sn in SnCl4, SnBr4, and SnI4. *J. Chem. Phys.* **1974**, *60* (3), 1149–1157. https://doi.org/10.1063/1.1681126.

(79) Nagashima, T.; Tajima, S.; 長島隆夫; 田島祐行. On the Anisotropic Knight Shift of Nuclear Magnetic Resonance in Metallic Tin. **1968**.

(80) Prochowicz, D.; Franckevicius, M.; Cieslak, A. M.; Zakeeruddin, S. M.; Gratzel, M.; Lewinski, J. Mechanosynthesis of the Hybrid Perovskite CH3NH3PbI3: Characterization and the Corresponding Solar Cell Efficiency. *J. Mater. Chem. Mater. Energy Sustain.* **2015**, *3*, 20772–20777. https://doi.org/10.1039/C5TA04904K.

(81) Prochowicz, D.; Yadav, P.; Saliba, M.; Saski, M.; Zakeeruddin, S. M.; Lewinski, J.; Gratzel, M. Mechanosynthesis of Pure Phase

Mixed-Cation MAxFA1-XPbI3 Hybrid Perovskites: Photovoltaic Performance and Electrochemical Properties. *Sustain. Energy Fuels* **2017**, *1*, 689–693. https://doi.org/10.1039/C7SE00094D.

(82) Saski, M.; Prochowicz, D.; Marynowski, W.; Lewiński, J. Mechanosynthesis, Optical, and Morphological Properties of MA, FA, Cs-SnX3 (X = I, Br) and Phase-Pure Mixed-Halide MASnIxBr3–x Perovskites. *Eur. J. Inorg. Chem.* **2019**, *2019* (22), 2680–2684. https://doi.org/10.1002/ejic.201801506.

(83) Hong, Z.; Tan, D.; John, R. A.; Tay, Y. K. E.; Ho, Y. K. T.; Zhao, X.; Sum, T. C.; Mathews, N.; García, F.; Soo, H. S. Completely Solvent-Free Protocols to Access Phase-Pure, Metastable Metal Halide Perovskites and Functional Photodetectors from the Precursor Salts. *iScience* **2019**, *16*, 312–325. https://doi.org/10.1016/j.isci.2019.05.042.

(84) Ajjouri, Y. E.; Locardi, F.; Gélvez-Rueda, M. C.; Prato, M.; Sessolo, M.; Ferretti, M.; Grozema, F. C.; Palazon, F.; Bolink, H. J. Mechanochemical Synthesis of Sn(II) and Sn(IV) Iodide Perovskites and Study of Their Structural, Chemical, Thermal, Optical, and Electrical Properties. *Energy Technol.* 1900788. https://doi.org/10.1002/ente.201900788.

(85) Xu, J.; Wang, J.; Rakhmatullin, A.; Ory, S.; Fernández-Carrión, A. J.; Yi, H.; Kuang, X.; Allix, M. Interstitial Oxide Ion Migration Mechanism in Aluminate Melilite La1+xCa1–XAl3O7+0.5x Ceramics Synthesized by Glass Crystallization. *ACS Appl. Energy Mater.* **2019**, *2* (4), 2878–2888. https://doi.org/10.1021/acsaem.9b00224.

(86) Thurber, K. R.; Tycko, R. Measurement of Sample Temperatures under Magic-Angle Spinning from the Chemical Shift and Spin-Lattice Relaxation Rate of 79Br in KBr Powder. *J. Magn. Reson.* **2009**, *196* (1), 84–87. https://doi.org/10.1016/j.jmr.2008.09.019.

(87) Venkatachalam, S.; Schröder, C.; Wegner, S.; van Wüllen, L. The Structure of a Borosilicate and Phosphosilicate Glasses and Its Evolution at Temperatures above the Glass Transition Temperature: Lessons from in Situ MAS NMR. *Phys. Chem. Glas. - Eur. J. Glass Sci. AndTechnology Part B* **2014**, *55* (6), 280–287.

(88) Yamada, K.; Kuranaga, Y.; Ueda, K.; Goto, S.; Okuda, T.; Furukawa, Y. Phase Transition and Electric Conductivity of ASnCl3 (A = Cs and CH3NH3). *Bull. Chem. Soc. Jpn.* **1998**, *71* (1), 127–134. https://doi.org/10.1246/bcsj.71.127.

(89) Taylor, R. E.; Beckmann, P. A.; Bai, S.; Dybowski, C. 127I and 207Pb Solid-State NMR Spectroscopy and Nuclear Spin Relaxation in PbI2: A Preliminary Study. *J. Phys. Chem. C* **2014**, *118* (17), 9143–9153. https://doi.org/10.1021/jp5023423.

(90) Rosales, B. A.; Hanrahan, M. P.; Boote, B. W.; Rossini, A. J.; Smith, E. A.; Vela, J. Lead Halide Perovskites: Challenges and Opportunities in Advanced Synthesis and Spectroscopy. *ACS Energy Lett.* **2017**, *2* (4), 906–914. https://doi.org/10.1021/acsenergylett.6b00674.

(91) Mitchell, M. R.; Reader, S. W.; Johnston, K. E.; Pickard, C. J.; Whittle, K. R.; Ashbrook, S. E. 119Sn MAS NMR and First-Principles Calculations for the Investigation of Disorder in Stannate Pyrochlores. *Phys. Chem. Chem. Phys.* **2010**, *13* (2), 488–497. https://doi.org/10.1039/C0CP01274B.

(92) Bagno, A.; Casella, G.; Saielli, G. Relativistic DFT Calculation of 119Sn Chemical Shifts and Coupling Constants in Tin Compounds. *J. Chem. Theory Comput.* **2006**, *2* (1), 37–46. https://doi.org/10.1021/ct050173k.

(93) Sharp, R. R. Rotational Diffusion and Magnetic Relaxation of 119Sn in Liquid SnCl4 and SnI4. *J. Chem. Phys.* **1972**, *57* (12), 5321–5330. https://doi.org/10.1063/1.1678224.

(94) Van Gompel, W. T. M.; Herckens, R.; Reekmans, G.; Ruttens, B.; D'Haen, J.; Adriaensens, P.; Lutsen, L.; Vanderzande, Dirk. Degradation of the Formamidinium Cation and the Quantification of the Formamidinium-Methylammonium Ratio in Lead Iodide Hybrid Perovskites by Nuclear Magnetic Resonance Spectroscopy. *J. Phys. Chem. C* **2018**, *122*, 4117–4124. https://doi.org/10.1021/acs.jpcc.7b09805.

(95) Dang, Y.; Zhou, Y.; Liu, X.; Ju, D.; Xia, S.; Xia, H.; Tao, X. Formation of Hybrid Perovskite Tin Iodide Single Crystals by Top-Seeded Solution Growth. *Angew. Chem.-Int. Ed.* **2016**, *55* (10), 3447–3450. https://doi.org/10.1002/anie.201511792.

(96) Chung, I.; Song, J.-H.; Im, J.; Androulakis, J.; Malliakas, C. D.; Li, H.; Freeman, A. J.; Kenney, J. T.; Kanatzidis, M. G. CsSnI3: Semiconductor or Metal? High Electrical Conductivity and Strong Near-Infrared Photoluminescence from a Single Material. High Hole Mobility and Phase-Transitions. *J. Am. Chem. Soc.* **2012**, *134* (20), 8579–8587. https://doi.org/10.1021/ja301539s.

(97) Kofod, P. Lineshapes of a Spin-12 Nucleus with Scalar Coupling to a Quadrupolar Nucleus Subject to Random Field Relaxation. *J. Magn. Reson. A* **1996**, *119* (2), 219–224. https://doi.org/10.1006/jmra.1996.0076.

(98) Phase Transitions in CsSnCl3 and CsPbBr3 An NMR and NQR Study : Zeitschrift für Naturforschung A https://www.degruyter.com/view/j/zna.1991.46.issue-4/zna-1991-0406/zna-1991-0406.xml (accessed Aug 23, 2019).

(99) Mosca, R.; Ferro, P.; Besagni, T.; Calestani, D.; Chiarella, F.; Licci, F. Effect of Humidity on the a.c. Impedance of CH3NH3SnCl3 Hybrid Films. *Appl. Phys. A* **2011**, *104* (4), 1181–1187. https://doi.org/10.1007/s00339-011-6407-z.

(100) Agashe, C.; Major, S. S. Effect of F, Cl and Br Doping on Electrical Properties of Sprayed SnO2 Films. *J. Mater. Sci. Lett.* **1996**, *15* (6), 497–499. https://doi.org/10.1007/BF00275412.

(101) Bloembergen, N.; Rowland, T. J. On the Nuclear Magnetic Resonance in Metals and Alloys. *Acta Metall.* **1953**, *1* (6), 731–746. https://doi.org/10.1016/0001-6160(53)90033-9.

(102) Borsa, F.; Barnes, R. G. Temperature Dependence of the Isotropic and Anisotropic Knight Shift in Polycrystalline Cadmium and β-Tin. *J. Phys. Chem. Solids* **1966**, *27* (3), 567–573. https://doi.org/10.1016/0022-3697(66)90200-9.

(103) Leijtens, T.; Prasanna, R.; Gold-Parker, A.; Toney, M. F.; McGehee, M. D. Mechanism of Tin Oxidation and Stabilization by Lead Substitution in Tin Halide Perovskites. *ACS Energy Lett.* **2017**, *2* (9), 2159–2165. https://doi.org/10.1021/acsenergylett.7b00636.

(104) Korringa, J. Nuclear Magnetic Relaxation and Resonance Line Shift in Metals. *Physica* **1950**, *16* (7), 601–610. https://doi.org/10.1016/0031-8914(50)90105-4.

(105) Kowalewski, J.; Maler, L. Nuclear Spin Relaxation in Liquids: Theory, Experiments, and Applications, Second Edition https://www.crcpress.com/Nuclear-Spin-Relaxation-in-Liquids-Theory-Experiments-and-Applications/Kowalewski-Maler/p/book/9781498782142 (accessed Aug 16, 2019).

(106) Abragam, A. *The Principles of Nuclear Magnetism*; Clarendon Press, 1961.

(107) Grutzner, J. B.; Stewart, K. W.; Wasylishen, R. E.; Lumsden, M. D.; Dybowski, C.; Beckmann, P. A. A New Mechanism for Spin−Lattice Relaxation of Heavy Nuclei in the Solid State: 207Pb Relaxation in Lead Nitrate. *J. Am. Chem. Soc.* **2001**, *123* (29), 7094–7100. https://doi.org/10.1021/ja0040924.

(108) Neue, G.; Bai, S.; Taylor, R. E.; Beckmann, P. A.; Vega, A. J.; Dybowski, C. 119Sn Spin-Lattice Relaxation in Alpha-SnF2. *Phys. Rev. B* **2009**, *79* (21), 214302. https://doi.org/10.1103/PhysRevB.79.214302.

(109) Shmyreva, A. A.; Safdari, M.; Furó, I.; Dvinskikh, S. V. NMR Longitudinal Relaxation Enhancement in Metal Halides by Heteronuclear Polarization Exchange during Magic-Angle Spinning. *J. Chem. Phys.* **2016**, *144* (22), 224201. https://doi.org/10.1063/1.4953540.

(110) Yamada, K.; Nose, S.; Umehara, T.; Okuda, T.; Ichiba, S. 81Br NQR and 119Sn Mössbauer Study for MSnBr3 (M=Cs and CH3NH3). *Bull. Chem. Soc. Jpn.* **1988**, *61* (12), 4265–4268. https://doi.org/10.1246/bcsj.61.4265.

(111) Onoda-Yamamuro, N.; Matsuo, T.; Suga, H. Thermal, Electric, and Dielectric Properties of CH3NH3SnBr3 at Low Temperatures. *J. Chem. Thermodyn.* **1991**, *23* (10), 987–999. https://doi.org/10.1016/S0021-9614(05)80179-X.

(112) Yamada, K.; Kawaguchi, H.; Matsui, T.; Okuda, T.; Ichiba, S. Structural Phase Transition and Electrical Conductivity of the Perovskite CH3NH3Sn1-XPbxBr3 and CsSnBr3. *Bull. Chem. Soc. Jpn.* **1990**, *63* (9), 2521–2525. https://doi.org/10.1246/bcsj.63.2521.

(113) Van Kranendonk, J.; Walker, M. Theory of Quadrupolar Nuclear Spin-Lattice Relaxation Due to Anharmonic Raman Phonon Processes. *Phys. Rev. Lett.* **1967**, *18* (17), 701–703. https://doi.org/10.1103/PhysRevLett.18.701.

(114) Pérez-Osorio, M. A.; Lin, Q.; Phillips, R. T.; Milot, R. L.; Herz, L. M.; Johnston, M. B.; Giustino, F. Raman Spectrum of the Organic–Inorganic Halide Perovskite CH3NH3PbI3 from First Principles and High-Resolution Low-Temperature Raman Measurements. *J. Phys. Chem. C* **2018**, *122* (38), 21703–21717. https://doi.org/10.1021/acs.jpcc.8b04669.

(115) Kuku, T. A. Ionic Conductivity of SnI2. *Solid State Ion.* **1986**, *20* (3), 217–222. https://doi.org/10.1016/0167-2738(86)90218-3.

(116) Futscher, M. H.; Lee, J. M.; McGovern, L.; Muscarella, L. A.; Wang, T.; Haider, M. I.; Fakharuddin, A.; Schmidt-Mende, L.; Ehrler, B. Quantification of Ion Migration in CH3NH3PbI3 Perovskite Solar Cells by Transient Capacitance Measurements. *Mater. Horiz.* **2019**. https://doi.org/10.1039/C9MH00445A.

(117) Ansel, D.; Debuigne, J.; Denes, G.; Pannetier, J.; Lucas, J. About SnF2 Stannous Fluoride V.: Conduction Characteristics. *Berichte Bunsenges. Für Phys. Chem.* **1978**, *82* (4), 376–380. https://doi.org/10.1002/bbpc.197800067.

(118) Shi, T.; Zhang, H.-S.; Meng, W.; Teng, Q.; Liu, M.; Yang, X.; Yan, Y.; Yip, H.-L.; Zhao, Y.-J. Effects of Organic Cations on the Defect Physics of Tin Halide Perovskites. *J. Mater. Chem. A* **2017**, *5* (29), 15124–15129. https://doi.org/10.1039/c7ta02662e.

(119) Yang, D.; Ming, W.; Shi, H.; Zhang, L.; Du, M.-H. Fast Diffusion of Native Defects and Impurities in Perovskite Solar Cell Material CH3NH3PbI3. *Chem. Mater.* **2016**, *28* (12), 4349–4357. https://doi.org/10.1021/acs.chemmater.6b01348.

(120) Lai, M.; Obliger, A.; Lu, D.; Kley, C. S.; Bischak, C. G.; Kong, Q.; Lei, T.; Dou, L.; Ginsberg, N. S.; Limmer, D. T.; et al. Intrinsic Anion Diffusivity in Lead Halide Perovskites Is Facilitated by a Soft Lattice. *Proc. Natl. Acad. Sci.* **2018**, *115* (47), 11929–11934. https://doi.org/10.1073/pnas.1812718115.

(121) Elmelund, T.; Scheidt, R. A.; Seger, B.; Kamat, P. V. Bidirectional Halide Ion Exchange in Paired Lead Halide Perovskite Films with Thermal Activation. *ACS Energy Lett.* **2019**, *4* (8), 1961–1969. https://doi.org/10.1021/acsenergylett.9b01280.

TOC:

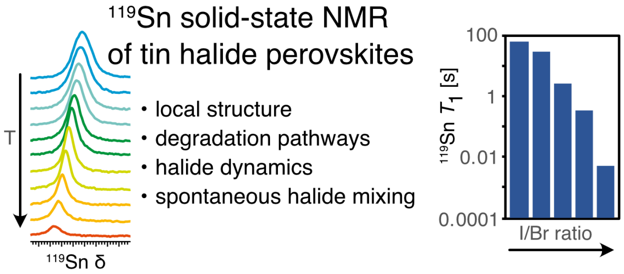
^{119}Sn solid-state NMR
of tin halide perovskites
• local structure
• degradation pathways
• halide dynamics
• spontaneous halide mixing
T
^{119}Sn δ
100
1
0.01
0.0001
^{119}Sn T_1 [s]
I/Br ratio